International Communications in Heat and Mass Transfer 167 (2025) 109207

Contents lists available at ScienceDirect

International Communications in Heat and Mass Transfer

journal homepage: www.elsevier.com/locate/ichmt

Design and validation of a lattice Boltzmann method with real properties for single-bubble boiling simulation

Ivan Talão Martins [a,b,*], Luben Cabezas Gómez [a], Pablo Fariñas Alvariño [b]

[a] Department of Mechanical Engineering, Heat Transfer Research Group, São Carlos School of Engineering (EESC), University of São Paulo (USP), Av. Trabalhador Sao-carlense, 400, São Carlos, 13561-250, São Paulo, Brazil

[b] Universidade da Coruña (UDC), Campus Industrial de Ferrol, Rúa Mendizábal s/n, Ferrol, 15403, A Coruña, Spain

ARTICLE INFO

Keywords:
Lattice Boltzmann method
Phase-field LBM
Saturated boiling simulation
Validation with experiments
Saturated HFE7100

ABSTRACT

This work reports a phase-field LBM model specifically designed to operate with real physical properties. The LBM will be applied to study the boiling phenomena involved in single bubbles' life-cycle of saturated HFE7100. Previous references on LBM with physical properties are scarce and, therefore, conducting a rigorous assessment of the method becomes of utmost importance. The model was first confronted to the Stefan problem, and numerical results match with outstanding accuracy with the analytical solution. This research goes on with a benchmark-exercise on experimental single-bubble-growth in saturated HFE7100 at 195 kPa and 5.1 K of superheating. Experiments with 19 bubbles yielded the most plausible shape, equivalent radius, apparent contact angle, dry radius, and forces acting on the typical bubble. Numerical results are reported in the proper manner to compare with all previously mentioned experimental features. This kind of comparison can be hardly found in the open literature, even though it potentially identify the physical mechanism responsible for any eventual numerical failure. The proposed LBM model reproduced the experimental data with great precision. This research will show that numerical results matched the experimental data within the uncertainty reported for almost the entire bubble life-cycle period.

1. Introduction

Boiling heat transfer is an energy transfer mechanism that take place in many daily natural processes as well as in several industrial applications. Some examples of man-made applications are industrial boilers, nuclear reactors, evaporators of power plants and refrigeration systems, heat pipes, electronic equipment, sprays, and others [1]. The boiling heat transfer phenomenon is commonly related to the evaporation of a fluid due to a driven temperature difference between a wall and a fluid caused by a heat transfer interaction. Among the various boiling processes, the pool boiling, is a boiling mechanism that frequently occurs in applications. Some non-extensive examples of industrial processes are the cooling of immersed electronic devices, quenching processes, refrigeration and power evaporators, nuclear boiling reactors, among many others devices. Following Carey [1], the pool boiling is defined as a process at the body surface immersed in a large volume of fluid, characterized by high heat transfer rates, especially in the nucleate boiling regime, where vapor bubbles form, growth and detach during the process of phase change.

In the last decades, a numerical method has drawn attention due to its potential to simulate a variety of considerable complex flows, such as single and multiphase isothermal flows, flows in porous medium, phase-change processes due to heat and mass transfer, and compressible flows, among other applications [2]. This method, called the lattice Boltzmann method (LBM), was initially derived from lattice gas cellular automata (LGCA) and is formally based on the discretization of the Boltzmann transport equation (BTE) in the phase space [3,4].

There are several LBM models developed to simulate multiphase and multicomponent flows, considering or not the phase change phenomena. These methods can be classified into four principal kinds: the color-gradient model [5–7], the pseudopotential method [8–10], the free energy method [11–13] and the phase-field-based models [14–17]. The last two kinds of methodologies are frequently classified as the same, as in Liu et al. [18], because both consider fundamental concepts related to fluid free energies to lead with the interface dynamics.

Addressing both phase segregation and interphase dynamics is necessary to model multiphase flows, which can be done by the use of intermolecular forces or derived from free energy theory [19]. This gives some advantage to the LBM to deal with multicomponent flows in comparison to the traditional methods, such as Volume-of-Fluid (VoF) or Level Set methods, mainly when these problems also include solid–fluid interactions [18]. Another advantage is that the LBM can deal

* Corresponding author at: Universidade da Coruña (UDC), Campus Industrial de Ferrol, Rúa Mendizábal s/n, Ferrol, 15403, A Coruña, Spain.
E-mail addresses: ivan.martins@udc.es (I.T. Martins), lubencg@sc.usp.br (L.C. Gómez), pablo.farinas@udc.es (P.F. Alvariño).

https://doi.org/10.1016/j.icheatmasstransfer.2025.109207

Available online 3 July 2025

Nomenclature

Acronyms

ABB	Anti-bounce-back
BB	Bounce-back
BC	Boundary condition
BGK	Bhatnagar–Gross–Krook
BTE	Boltzmann transport equation
EoS	Equation of State
HTC	Heat Transfer Coefficient
LBM	Lattice Boltzmann method
LGCA	Lattice gas cellular automata
MRT	Multiple-relaxation-time
NS	Navier–Stokes
VoF	Volume-of-Fluid

Greek Symbols

α	thermal diffusivity [$m^2\ s^{-1}$]
β	constant for free energy calculation [$J\ m^{-3}$]
β_T	thermal expansion coefficient [K^{-1}]
$\boldsymbol{\Lambda}$	collision matrix for the MRT collision operator
Δt	discrete time increment [s]
Δx	discrete space interval [m]
δ_{ini}	initial thermal boundary layer width [m]
ϵ	expansion coefficient for the Chapman–Enskog analysis
γ	coordinate perpendicular to the interface [m]
κ	constant for free energy calculation [N]
λ	parameter for the diffusive flux [m^{-1}]
μ	chemical potential [$N\ m^{-2}$]
ν	Kinematic viscosity [$m^2 s^{-1}$]
$\overline{\rho}$	mean density [$kg\ m^{-3}$]
ϕ	order parameter or liquid concentration
$\Pi_{\alpha\beta\gamma}$	parameter for NS Chapman–Enskog analysis [$m\ s^{-1}$]
Ψ	free energy [$J\ m^{-3}$]
ψ	source term for mass conservation equation [s^{-1}]
ρ	fluid density [$kg\ m^{-3}$]
σ	surface tension of the fluid [$N\ m^{-1}$]
τ	relaxation time for LBE [s]
φ	static contact angle [°]
φ_{ap}	apparent contact angle [°]
ξ	constant for analytical solution of the Stefan problem
ζ	dynamic viscosity [Pa s]

Roman Symbols

ΔT	superheating degree [K]
$\dot{m}'''$	volumetric vapor generation term [$kg\ m^{-3} s^{-1}$]
$\dot{q}''$	heat flux [$W\ m^{-2}$]
$\dot{Q}_s$	heat transfer rate at the surface [W]
$\mathbf{c}$	discrete velocity vector [$m\ s^{-1}$]
$\mathbf{F_b}$	buoyancy force [$N\ m^{-3}$]
$\mathbf{F_g}$	gravitational force [$N\ m^{-3}$
$\mathbf{F_s}$	interfacial force [$N\ m^{-3}$]
$\mathbf{F}$	external force [$N\ m^{-3}$]
$\mathbf{g}$	gravity acceleration [$m\ s^{-2}$]
$\mathbf{I}$	Identity matrix
$\mathbf{j}$	flux density between phases [$m\ s^{-1}$]
$\mathbf{M}$	transformation matrix
$\mathbf{m}$	moments of the distribution functions
$\mathbf{M}^{-1}$	inverse of the transformation matrix
$\mathbf{n}$	normal vector
$\mathbf{u}$	fluid velocity [$m\ s^{-1}$]
$\mathbf{x}$	position vector [m]
$\overline{q''}$	mean heat flux [$W\ m^{-2}$]
$\overline{h}$	mean heat transfer coefficient [$W\ m^{-2}K^{-1}$]
c	lattice speed [$m\ s^{-1}$]
c_p	specific heat at constant pressure [$J\ kg^{-1}K^{-1}$]
c_s	lattice sound speed [$m\ s^{-1}$]
E	error term on the Chapman–Enskog analysis
F_b	buoyancy force [N]
F_D	dynamic force [N]
F_x	force in x-cartesian direction [$N\ m^{-3}$]
F_y	force in y-cartesian direction [$N\ m^{-3}$]
F_σ	surface tension force [N]
F_{cp}	contact pressure force [N]
g_i	discrete distribution function for the pressure [$kg\ m^{-3}$]
h_i	discrete distribution function for the order parameter
h_{lg}	latent heat of vaporization [$J\ kg^{-1}$]
K	constant for correcting the vapor generation term
k	thermal conductivity [$W\ m^{-1}K^{-1}$]
Kn	Knudsen number
L	length of the domain [m]
M	mobility [$m^2\ s^{-1}$]
N_x	number of nodes in x direction
p	pressure [Pa]
P_r	reduced pressure
P_{abs}	absolute pressure [Pa]
q	number of discrete velocity directions of the lattice scheme
R_c	cavity radius [m]
R_d	dry radius [m]
R_{eq}	equivalent radius [m]
R_{ini}	initial bubble radius [m]
s_i	discrete temperature distribution function [K]
S_{g_i}	source term for the pressure LBE [$Kg\ m^{-3} s^{-1}$]
S_{h_i}	source term for the order parameter [s^{-1}]
S_{s_i}	source term for the thermal LBE [$K\ s^{-1}$]
T	temperature [K]
t	time [s]

T^*	normalized temperature [K]
T_r	reduced temperature
T_{ref}	reference temperature for buoyancy force [K]
u	fluid velocity at x-cartesian direction [m s^{-1}]
V	bubble volume [m^3]
v	fluid velocity at y-cartesian direction [m s^{-1}]
W	interface width [m]
w	weight functions
x_i	interface velocity for the Stefan problem [m]
A	constant for the contact angle model

Subscripts/superscripts

$*$	post-collision variables
ν	referent to the pressure LBE
$\bar{i}$	discrete velocity direction opposite to i
ϕ	relative to order parameter LBE
b	referent to the boundary node
eq	indicates the equilibrium distribution function
g	saturated vapor, gas phase
i	discrete velocity directions
j	nodes in x direction
k	subindex indicating which component the variable is related to
l	saturated liquid
$q2$	referent to the fourth relaxation time in the relaxation matrix
sat	saturated state
T^*	relative to the thermal LBE
w	variables at the boundary wall

with the transition between the different boiling regimes automatically, as the bubble merging process occurs naturally by mesoscale interactions [20].

The multiphase LBM model that has been the most used to simulate vapor–liquid phase change problems with heat transfer is the pseudopotential model [20]. This model has been extensively used for simulating several liquid–gas two-phase one-component problems. For example, stationary droplet evaporation, nucleate pool boiling in cavities and channels [21–24], flow boiling [25–27], gas–liquid condensation [28], cavitation [29], and other processes. Recent works have been also applied the pseudopotential LBM for simulating more complexes phenomena, such as liquid–gas phase-change process considering effects of electric fields [30,31], which evidence the capability of this model.

Nevertheless, the simulation of liquid–vapor phase-change heat transfer processes for real conditions with the pseudopotential LBM is complicated [32]. They showed the necessity of performing mesh refinement to correctly assess pool boiling problems with the LBM, demonstrating also the nucleate pool boiling results' dependence on contact angle. The authors observed that the simulation of pool boiling problems considering real experimental conditions would require very small mesh size to obtain numerical convergence. This fact, not well addressed in the open literature, greatly influences the use of pseudopotential LBM for simulating real boiling problems.

For example, recently Wang et al. [33] developed a conversion strategy to simulate liquid–vapor phase change with the pseudopotential method. The authors proposed conversion relations for the fundamental units using the surface tension and EoS parameters related to fluid properties, to deduce conversion relations of other quantities. They simulated film evaporation and single bubble nucleation from a V-shaped cavity, recovering the latent heat of the fluid and the correct critical superheat temperature in physical units, respectively. However, in both cases they employed mesh sizes between 2400 and 120000 lattices (120×20 and 300×400, respectively), and also assumed that the liquid and vapor kinematic viscosities were equal ($\nu_g = \nu_l = 1.29 \cdot 10^{-7}$ $m^2 s^{-1}$).

In addition, the pseudopotential LBM needs the use of an equation of state (EoS), limiting the applicability of the method for medium to high density ratios, corresponding to medium or low saturation temperatures. A recent work uses a piece-wise linear EoS [34], only valid for the tuned fluid like water, in this case. Zheng et al. [35] proposed a thermal pseudopotential model for simulating problems considering the full set of properties for a real fluid, converting the physical variables to the lattice units. They employed the more accurate Martin-Hou EoS and also a multi-block grid for improving the model estimations. However due to the necessity of finer meshes they solved liquid–vapor phase change problems for higher reduced temperature values, from 0.9 to 0.98 approximately, and at nanoscales.

Although the pseudopotential LBM is the most employed for simulating phase-change processes, the phase-field-based LBM models are the kind of multiphase LBM that presented better results when handling with high density ratios and, consequently, real fluids, see Martins et al. [36]. By this reason these models were chosen as the basis for the development of our methodology, focusing in the simulation of thermal liquid–gas phase-change problem considering exactly the same operational conditions found in experiments.

The original free energy based method was developed in the end of the 20th century, with the works of Swift et al. [11], Orlandini et al. [12], Swift et al. [13], based on the Van der Waals EoS. In the beginning of the 21st century, some authors developed a multicomponent LBM based on the original Swift model [37–43], but using the square gradient form of the free energy, or Helmholtz energy [44].

The first version of the phase-field model was published by He et al. [14], proposing the use of two distribution functions to recover the momentum and mass conservation equations for a multiphase system. For this task, the authors assume each phase as incompressible and employ two distribution functions, one to deal with the pressure distribution and other for mass conservation. Their models became the foundation for more elaborated methods on phase-field theory, as it will be possible to see below.

This method was further modified by Zheng et al. [16] to simulate multiphase flows with high density ratio, considering the recovering of the Cahn–Hilliard equation to track the interface between the different phases. Further, this method was adapted to consider the liquid–gas phase-change phenomena in the works of Dong et al. [45,46]. The same procedure was used by Sun et al. [47], Sun [48] to simulate single bubble nucleate boiling, and their results were compared qualitatively with experimental data.

However, as pointed by Fakhari and Rahimian [49],Liang et al. [50], the [16] model is only valid to density matched situations, because the method is incapable to distinguish between two different cases with the same mean density. For example, if in one system the liquid and gas phase densities are $\rho_l = 501.0$ kg m^{-3} and $\rho_g = 500.0$ kg m^{-3}, respectively, and in other system they are $\rho_l = 1000.0$ kg m^{-3} and $\rho_g = 1.0$ kg m^{-3}, both have the same mean density of $\overline{\rho} = 500.50$ kg m^{-3}. Then, as the momentum conservation part of the Zheng et al. [16] method is based on the average density of the fluid, both systems will present the same results in the simulations, which is not necessarily what would happened in a real system.

Thereby, Fakhari and Rahimian [49] proposed an incompressible modification to the pressure distribution function, used to recover the Navier–Stokes (NS) equation similar to the [14] procedure, trying to avoid the density complications of Zheng et al. [16] model. A similar method was also proposed by Zu and He [51] to deal with high density ratio multiphase multi-component flows.

Moreover, Lee and Lin [17], Lee et al. [52], Lee and Fischer [53] proposed a two-phase multicomponent LBM to simulate high density ratio problems, trying to eliminate the presence of parasitic currents. In the sequence, Amaya-Bower and Lee [54], Lee [55], Lee and Liu [56] improved the previous models, which were further used to simulate thermal liquid–gas phase change by Safari et al. [57,58].

Other authors also performed phase-change simulations with Lee and Liu [56] models, such as Begmohammadi et al. [59], Sadeghi et al. [60]. Nonetheless, this model presents some complications about the non-conservation of the domain mass, which is induced by the mixed derivatives employed to calculate the spatial gradients, a combination of central and biased finite difference schemes [61].

In the sequence, some authors developed improved models also for high density ratio problems, but now trying to recover the conservative Allen–Cahn equation for the interface-tracking, instead of Cahn–Hilliard equation [62–65]. Again, these models were also improved to consider the thermal liquid–gas phase change phenomena, as can be seen in Haghani-Hassan-Abadi et al. [66], He et al. [67].

However, the great majority of the works did not consider real fluids in their simulations, some of them even use densities close to real ones, but with different viscosity and surface tension values, and generally the density ratio does not surpass 1000/1. This can be far from the reality when dealing with fluids such as water, for which these ratios can attain values of 43000 and 470 for the density and kinematic viscosity, as considered in Martins et al. [36]. At the best knowledge of the authors, there are no published works capable of embracing the pool boiling phenomena in a real installation. This fact evidences that it is still a challenge the simulation of real boiling problems with the LBM, limiting the applicability of the method. This limitation of the LBM is faced and reduced in the present research and, perhaps, it constitutes the main contribution of this work.

As a general rule, in the LBM community, comparisons are made qualitatively through observation of the bubble shape reported by the numerical algorithm and the experimental facility, as in the following works [48,68–70]. Regretfully, numerical–experimental comparison with additional quantitative information is usually omitted since, in most cases, numerical scientists cannot find available additional and/or detailed experimental information.

Recall that bubble growth is governed by coupled mechanisms that take place simultaneously. Provide the whole set of experimental information, along with the corresponding uncertainty, is quite useful for numerical scientists. Numerical methods can also provide the whole set of information, and therefore, an step-by-step assessment is pertinent to disaggregate the mechanisms involved in the bubble growth. This information becomes necessary to identify why and when the numerical algorithm might be eventually failing. As a result, more detailed experimental evidence is both necessary and pertinent for the eventual assessment of numerical methods.

This research reports a phase-field LBM that overcomes previous limitations, since the model will be able to simulate the physical true conditions in an experimental rig on pool boiling. This work will take advantage of previous work from the authors [36], and push their model forward to solve a single-bubble boiling of saturated HFE7100 directly in physical units, considering the full set of variables at the experiment conditions. Therefore, this work reports (i) a new methodology to simulate any/all eventual real pool boiling phenomena and (ii) a quantitative benchmark exercise with the results yielded by an experimental facility subject to equal operating conditions.

The procedure is first validated through the Stefan problem, comparing the numerical and analytical solutions. This problem also serves as a calibration test for the vapor generation term, as will be explained in Section 2. In the sequence, the results of single-bubble pool boiling will be exhaustively and quantitatively compared against experimental results.

The experimental data were obtained in the workbench presented in Alvariño et al. [71], considering a single-bubble nucleating boiling of saturated HFE7100 at 195 kPa and 5.1 K of superheating. To our best knowledge HFE7100 experimental data at this pressure are very scarce in the open literature. Thus, we can also consider that we are presenting new experimental data which can be employed for comparison purpose by other researchers. In fact, it may be difficult to find numerical–experimental studies that provide a comparison of results at the pressure–temperature values presented in the paper. Furthermore, the experimental data are treated with a procedure recently published in Martins et al. [72]. From this procedure, we can determinate a characteristic bubble that represents the entire set of bubbles analyzed in the experiment for one given condition, as well as its respective uncertainties. Consequently, this set of quantitative data about bubble's characteristics allows the comparison and validation of the numerical results, a task very difficult to be found in the open literature.

2. Methodology

For modeling the fluid dynamics and phase separation, we adopt the phase-field LBM model based on the conservative Allen–Cahn equation with the dimensional approach proposed by Martins et al. [36]. This approach employs the LBEs, the collision operators, and the calculation of macroscopic variables using Δt, Δx and c in physical units when necessary, to ensure that all variables are used in physical units during simulations. Then, all the variables can be used directly in its physical units. For example, the relaxation time is $\tau = \nu/c_s^2 + 0.50\Delta t$, the ν is kept in m^2/s, $c_s^2 = c^2\sqrt{1/3} = (\Delta x/\Delta t)^2\sqrt{1/3}$ in m^2/s^2, Δt in s and Δx in m. Then, the final dimension of τ is s. Similarly, all other variables such as f, $\mathbf{u}$, ρ, $\mathbf{c}_i$ are kept in physical units and the whole simulation is performed in the physical space. So, there is no need for unit conversion in the beginning or in the end of the simulation. For more information on this process, see Martins et al. [36].

The LBM model used here is also based on the approaches of Liang et al. [50], Sugimoto et al. [73] with modifications for accounting the phase-change process due to temperature change. Then, the full methodology proposed here for the simulation of boiling phenomena consists of these modified models, as well as new treatments for the liquid–gas thermal interface, gravity force and boundary conditions. The methodology is applied employing the dimensional approach, see Martins et al. [36], which allows to simulate the problem directly in physical units, without need of any conversion to lattice units, and thus, facilitating the reproduction of the true physical operating conditions in any experimental rig or industrial process.

2.1. Allen–Cahn-based lattice Boltzmann method

The phase-field LBM based on the conservative Allen–Cahn equation adopts two distribution functions: one for the pressure field, g_i, and other for the order parameter (or liquid concentration), h_i, representing the mass conservation for the liquid phase.

Starting by the order parameter distribution function, first we need to derive the conservative Allen–Cahn equation. Considering the mass conservation equation for each component, k, with a source term ψ [74], being ρ the fluid density, $\mathbf{u}$ the fluid velocity and $\mathbf{j_k}$ the flux density between the phases [75], we have the following equation,

$$\partial_t \rho_k + \nabla \cdot (\rho_k \mathbf{u}) = \nabla \cdot (\rho_k \mathbf{j_k}) + \rho_k \psi_k. \tag{1}$$

The flux densities are divided into two main sources [76]: the diffusive flux, $\mathbf{j_D} = M\nabla\phi$, and the phase separation flux, $\mathbf{j_P} = -M\lambda\mathbf{n}$. Here, M is the mobility coefficient, representing the diffusive ratio between the phases, λ is a parameter defined as $\lambda = 4\phi(1-\phi)/W$ and ϕ is the order parameter, assuming 1 for the liquid phase and 0 for the gas phase. In these expressions, W stands for the interface width and $\mathbf{n}$, for the normal vector to the interface, pointing into the liquid phase.

The local density of the system is related to the order parameter by $\rho = \rho_l\phi + (1-\phi)\rho_g$, where ρ_l and ρ_g are the liquid and gas phase densities, respectively. The normal vector can be calculated as follows:

$\mathbf{n} = \nabla\phi/|\nabla\phi|$. Taking the liquid phase conservation equation, i.e. $k = l$, adding the vapor source term due to thermal phase-change process, $\dot{m}'''$ (kg m^{-3}s^{-1}), and inserting the previous definitions in Eq. (1), we obtain the Allen–Cahn equation with the source term for evaporation:

$$\partial_t\phi + \nabla\cdot(\phi\mathbf{u}) = \nabla\cdot\left[M\left(\nabla\phi - \frac{4\phi(1-\phi)}{W}\mathbf{n}\right)\right] - \frac{\dot{m}'''}{\rho_l}. \tag{2}$$

For correctly recovering Eq. (2), we employ the lattice Boltzmann equation (LBE) for h_i with the BGK collision operator, presented in Eq. (3). In this equation, $\mathbf{x}$ is the position vector, h_i^{eq} is the equilibrium distribution functions, S_{h_i} is the source term and τ_ϕ is the relaxation time, related to the mobility by $M = c_s^2\left(\tau_\phi - 0.5\Delta t\right)$ for correctly recovering the Eq. (2) through the Chapman–Enskog analysis [77]. This analysis is shown in Appendix A.1.

$$h_i(\mathbf{x}+\mathbf{c_i}\Delta t, t+\Delta t) - h_i(\mathbf{x},t) = -\frac{\Delta t}{\tau_\phi}\left[h_i(\mathbf{x},t) - h_i^{eq}(\mathbf{x},t)\right] + \left(1 - \frac{\Delta t}{2\tau_\phi}\right)S_{h_i}(\mathbf{x},t)\Delta t \tag{3}$$

The equilibrium distribution functions are defined by Eq. (4), where w_i are the weights and $\mathbf{c_i}$ are the lattice velocities.

$$h_i^{eq} = w_i\phi\left[1 + \frac{\mathbf{c}_i\cdot\mathbf{u}}{c_s^2}\right] \tag{4}$$

For all two-dimensional (2D) simulations, the D2Q9 velocity scheme was employed. Only for the 1D problem we used the D1Q3 scheme. Thus, according to Qian et al. [78] the sound speed in the lattice cells for both arrangements is $c_s = c\sqrt{1/3}$, where c is the lattice speed defined as $c = \Delta x/\Delta t$. In this expression, Δx stands for the grid discrete interval while Δt, for the temporal interval between the time steps. For this specific velocity scheme, the weights and the lattice velocity can be defined by Eqs. (5) and (6), respectively. In the case of the D1Q3, these values change to $w_i = (4/6;\ 1/6;\ 1/6)$ and $\mathbf{c_i} = c\,(0,\ 1,\ -1)$.

$$w_i = \begin{cases} 4/9 & , \text{ if } i = 0; \\ 1/9 & , \text{ if } i = 1,2,3,4; \\ 1/36 & , \text{ if } i = 5,6,7,8; \end{cases} \tag{5}$$

$$\mathbf{c_i} = c\begin{cases} (0,0) & , \text{ if } i = 0; \\ (1,0),(0,1),(-1,0),(0,-1) & , \text{ if } i = 1,2,3,4; \\ (1,1),(-1,1),(-1,-1),(1,-1) & , \text{ if } i = 5,6,7,8; \end{cases} \tag{6}$$

In the present model we modified the source term for accounting the effects of vapor generation due to temperature-change, $\dot{m}'''$, resulting in Eq. (7).

$$S_{h_i} = w_i\left\{\frac{\mathbf{c_i}\cdot\left[\partial_t(\phi\mathbf{u}) + c_s^2\frac{4\phi(1-\phi)}{W}\mathbf{n}\right]}{c_s^2} - \frac{\dot{m}'''}{\rho_l}\right\} \tag{7}$$

At last, the order parameter is calculated from the distribution functions according to Eq. (8), where q represents the number of discrete velocity directions of the scheme (e.g. 9, for the D2Q9 scheme). Notably, this expression was also modified to account the mass source term $\dot{m}'''$. Then, the local density, ρ, and dynamic viscosity, ζ, can be calculated as a linear function of ϕ: $\rho = \phi\rho_l + (1-\phi)\rho_g$ and $\zeta = \phi\zeta_l + (1-\phi)\zeta_g$.

$$\phi = \sum_{i=0}^{q-1} h_i - \frac{\Delta t}{2}\frac{\dot{m}'''}{\rho_l} \tag{8}$$

Considering now the pressure distribution function, in order to improve the stability of the method we used the MRT collision operator. Then, we define the LBE for the pressure dynamics by Eq. (9), where $[\mathbf{M}]$ is the transformation matrix, responsible for transforming the functions to the momentum space, $\boldsymbol{\Lambda}$ is the collision matrix, which has the relaxation rates for each momentum, S_{g_j} is the source term and $[\mathbf{I}]$ is the identity matrix. It is important to mention that, for developing this LBE, the fluid was assumed to be incompressible.

$$\begin{aligned} g_i(\mathbf{x}+\mathbf{c}_i\Delta t, t+\Delta t) - g_i(\mathbf{x},t) = &-\Delta t\left[\mathbf{M}^{-1}\boldsymbol{\Lambda}\mathbf{M}\right]_{ij}\left[g_j(\mathbf{x},t) - g_j^{eq}(\mathbf{x},t)\right] \\ &+ \Delta t\mathbf{M}_{ij}^{-1}\left(I_{ij} - \frac{\Delta t\boldsymbol{\Lambda}_{ij}}{2}\right)\mathbf{S}_{g_j}(\mathbf{x},t) \end{aligned} \tag{9}$$

It is convenient for the implementation to calculate the collision directly in the moment space. For this task, first we transform the distribution functions and the source term to the moment space using the transformation matrix. Then, the collision can be performed by Eq. (10), where $\mathbf{m}^*$ are the post-collision moments. In the sequence, the post-collision distribution functions are obtained by $\mathbf{g}^*(\mathbf{x},t) = [\mathbf{M}]^{-1}\cdot\mathbf{m}^*(\mathbf{x},t)$, followed by the propagation of the functions: $g_i(\mathbf{x}+\mathbf{c}_i\Delta t, t+\Delta t) = g_i^*(\mathbf{x},t)$.

$$\mathbf{m}^*(\mathbf{x},t) = \mathbf{m}(\mathbf{x},t) - \Delta t\,[\boldsymbol{\Lambda}]\cdot\left[\mathbf{m}(\mathbf{x},t) - \mathbf{m}^{eq}(\mathbf{x},t)\right] + \Delta t\left([I] - \frac{\Delta t}{2}[\boldsymbol{\Lambda}]\right)\cdot\mathbf{S_g}(\mathbf{x},t) \tag{10}$$

Regarding the collision in the moment space, the equilibrium moments are given by Eq. (11).

$$\begin{aligned} \mathbf{m}^{eq} = \{&0;\ 3(\rho\mathbf{u}\cdot\mathbf{u} + 2p);\ -3c^2(\rho\mathbf{u}\cdot\mathbf{u} + 3p); \\ &\rho u;\ -c^2\rho u;\ \rho v;\ -c^2\rho v;\ \rho\left(u^2 - v^2\right);\ \rho uv\} \end{aligned} \tag{11}$$

Additionally, to properly capture the gravity effects on the pressure field, we adopt the following expression for the body force, $\mathbf{F_g} = \rho\mathbf{g}$, which matches exactly to the gravity force in Eq. (15). This choice is based on an observation made by Czelusniak et al. [79], where they realize that the correct implementation of the gravitational forces is strongly related to the pressure gradients along the y direction, which is particularly important for modeling the fluid motion. It should be noted that various phase-field LBM works employ other formulations, as for example $\mathbf{F_g} = (\rho_g - \rho_l)\mathbf{g}$, $\mathbf{F_g} = (\rho - \rho_l)\mathbf{g}$ or $\mathbf{F_g} = (\rho - \overline{\rho})\mathbf{g}$ [51,66,67,80,81]. Depending on the values of $\mathbf{g}$ this kind of term can affect the pressure distribution in the computational domain, see Czelusniak et al. [79].

The buoyancy force in the liquid phase due to natural convection is also considered in our model. For this task, we employed the Boussinesq approach, $\mathbf{F_b} = -\mathbf{g}\rho_l\beta_T\left(T - T_{ref}\right)$, where β_t is the thermal expansion coefficient and T_{ref} is the reference temperature where β_T and ρ_l are measured [4]. In this paper, we took the saturation temperature as the reference ($T_{ref} = T_{sat}$). As in our model the vapor is assumed to remain at T_{sat}, the buoyancy force is not considered in this phase ($\mathbf{F_b} = \mathbf{0}$ at the gas phase).

Another modification of the traditional phase-field LBM is in the source term for the pressure distribution function. Here, we also need to add extra terms to insert the effects of vapor generation in the flow field, similar to in Sugimoto et al. [73]. In the moment space, this source term can be given by Eq. (12). Here $\mathbf{F} = \left(F_x, F_y\right)$ is the total force, involving $\mathbf{F_g}$, $\mathbf{F_s}$ and $\mathbf{F_b}$.

$$\begin{aligned} \mathbf{S_g} = \{&\nabla\rho\cdot\mathbf{u} + \rho\dot{m}'''\left(\rho_g^{-1} - \rho_l^{-1}\right);\ -2c^2\rho\dot{m}'''\left(\rho_g^{-1} - \rho_l^{-1}\right); \\ &c^4\left[\rho\dot{m}'''\left(\rho_g^{-1} - \rho_l^{-1}\right) - \nabla\rho\cdot\mathbf{u}\right]; \\ &F_x;\ -c^2F_x;\ F_y;\ -c^2F_y;\ \frac{2}{3}c^2\left(u\partial_x\rho - v\partial_y\rho\right);\ \frac{1}{3}c^2\left(v\partial_x\rho + u\partial_y\rho\right)\} \end{aligned} \tag{12}$$

After the collision and the streaming processes, the macroscopic velocity and the pressure field can be calculated by the moments of g_i, using Eq. (13) and Eq. (14), respectively. Again, the traditional Allen–Cahn-based LBM must be modified to include the effects of $\dot{m}'''$ in the pressure calculation. It is important to mention that here we adopt the relative pressure, for convenience, which is the difference between the saturation pressure and the absolute pressure, $p = P_{abs} - P_{sat}$.

$$\rho\mathbf{u} = \sum_{i=0}^{q-1}\mathbf{c_i}g_i + \frac{\Delta t}{2}\mathbf{F} \tag{13}$$

$$p = \frac{c_s^2}{1-w_0}\left\{\sum_{i\neq 0}^{q-1} g_i + \rho w_0\left[-\frac{\mathbf{u}\cdot\mathbf{u}}{2c_s^2}\right] + \frac{\Delta t}{2}\left[\mathbf{u}\cdot\nabla\rho + \left(1-w_0\right)\rho\dot{m}'''\left(\frac{1}{\rho_g}-\frac{1}{\rho_l}\right)\right]\right\} \tag{14}$$

At last, from the momentum LBE, Eq. (10), it is possible to recover the NS equation, represented by Eq. (15) [82], where ζ stands for the fluid dynamic viscosity. This recovering is performed by doing the Chapman–Enskog analysis, which can be seen in Appendix A.2.

Also, from this analysis we can relate the main values of the relaxation rates with the viscosity of the fluid. The relaxation matrix can be defined as $\boldsymbol{\Lambda} = \mathrm{diag}(\Delta t^{-1}, \Delta t^{-1}, \Delta t^{-1}, \Delta t^{-1}, \tau_{q2}^{-1}, \Delta t^{-1}, \Delta t^{-1}, \tau_{\nu}^{-1}, \tau_{\nu}^{-1})$. Then, they are related to the kinematic viscosity of the fluid, $\nu = \zeta/\rho$, by $\nu = c_s^2\left(\tau_\nu - 0.5\Delta t\right)$ and $\tau_{q2}^{-1} = \left(\frac{3}{\Delta t}\right)\frac{\left(2/\Delta t - \tau_\nu^{-1}\right)}{\left(3/\Delta t - \tau_\nu^{-1}\right)}$, see Martins et al. [36].

$$\partial_t(\rho\mathbf{u}) + \nabla\cdot(\rho\mathbf{u}\mathbf{u}) = -\nabla p + \nabla\cdot\left[\zeta\left(\nabla\mathbf{u} + \nabla\mathbf{u}^T\right)\right] + \rho\mathbf{g} + \mathbf{F_s} + \mathbf{F_b} \tag{15}$$

For the interface force, the potential form based on the chemical potential μ is adopted in this work [83], $\mathbf{F_s} = \mu\nabla\phi$, as it is commonly employed in the Allen–Cahn-based LBM models [50,63,84].

The chemical potential can be obtained from the free energy of the system [85], Ψ. Approaching the domain as a two-component system, besides being a single-component two-phase system, the chemical potential can be given by $\mu = \partial_\phi\Psi = 4\beta(\phi-1)(\phi-0.5) - \kappa\nabla^2\phi$, where β and κ are constants related to the interface width W and surface tension σ as in Eq. (16) [86]. This approach is convenient, as it facilitates the calculation of the interface force, and was used by other phase-change works using phase-field LBM models [16,50,56].

$$\beta = 12\frac{\sigma}{W}; \qquad \kappa = \frac{3}{2}\sigma W. \tag{16}$$

The first and second derivatives of ϕ are calculated using a central finite difference scheme, denoted by Eqs. (17) and (18). As density and order parameter are linearly related, the density gradient can be obtained from the order parameter gradient as $\nabla\rho = \left(\rho_l - \rho_g\right)\nabla\phi$. The temporal derivative of $\phi\mathbf{u}$ here is calculated using a second order backward finite difference scheme, as in Eq. (19).

$$\nabla\phi(\mathbf{x}) = \sum_{i\neq 0}\frac{w_i\mathbf{c_i}\phi(\mathbf{x}+\mathbf{c_i}\Delta t)}{c_s^2\Delta t} \tag{17}$$

$$\nabla^2\phi(\mathbf{x}) = \sum_{i\neq 0}\frac{2w_i\left[\phi(\mathbf{x}+\mathbf{c_i}\Delta t) - \phi(\mathbf{x})\right]}{c_s^2\Delta t^2} \tag{18}$$

$$\partial_t(\phi\mathbf{u})_{\mathbf{x},t} = \frac{3(\phi\mathbf{u})_{\mathbf{x},t} - 4(\phi\mathbf{u})_{\mathbf{x},t-\Delta t} + (\phi\mathbf{u})_{\mathbf{x},t-2\Delta t}}{2\Delta t} \tag{19}$$

An important feature that must be explained is how the interface is initialized at the beginning of the simulation, because a bad initial profile can lead to undesirable instabilities. As the LBM model assumes a diffuse interface between the phases, it is convenient to use an hyperbolic tangent profile to perform the initial values of ϕ, as given by Eq. (20). In this equation, $\gamma(\mathbf{x})$ denotes the coordinate perpendicular to the interface.

$$\phi(\mathbf{x},0) = \frac{1}{2} + \frac{1}{2}\tanh\left(\frac{2\gamma(\mathbf{x})}{W}\right) \tag{20}$$

2.2. Thermal lattice Boltzmann method

For modeling the temperature distribution of the domain, first we made some assumptions about the liquid–gas system:

1. The fluid is incompressible (as already assumed before);
2. The vapor phase remains at saturation temperature (T_{sat});
3. All the heat flux arriving at the interface is consumed in the phase-change process.

Then, by hypothesis 1 we only need to calculate the heat transfer at the liquid phase. For this task, we employed the traditional thermal lattice Boltzmann method considering the dimensional approach [36]. The method uses an additional distribution function, s_i, to determine the temperature field in the simulation. However, in the presence of the liquid–gas phase-change process, we need to add extra terms into the LBE to recover the complete energy conservation equation, represented by Eq. (21) for the liquid phase with constant local density, ρ_l, and constant specific heat, c_{p_l}. This is made through the source term, S_{s_i}.

$$\partial_t T^* + \mathbf{u}\cdot\nabla T^* = \alpha_l\nabla^2 T^* \tag{21}$$

Also, after the Chapman–Enskog analysis of Eq. (22), with the traditional source term the remaining error would be $\nabla\cdot\left(\tau_{T^*} - \Delta t/2\right)\epsilon\partial_t^{(1)}(T^*\mathbf{u})$. To mitigate its impact on the LBM solution, we also include the term $\partial_t(T^*\mathbf{u})$ in S_{s_i}, which reduces the error to $\nabla\cdot\left(\tau_{T^*} - \Delta t/2\right)\epsilon^2\partial_t^{(2)}(T^*\mathbf{u})$. Then, considering the BGK collision operator, the thermal LBE can be defined by Eq. (22).

$$s_i(\mathbf{x}+\mathbf{c_i}\Delta t, t+\Delta t) - s_i(\mathbf{x},t) = -\frac{\Delta t}{\tau_{T^*}}\left[s_i(\mathbf{x},t) - s_i^{eq}(\mathbf{x},t)\right] + \left(1-\frac{\Delta t}{2\tau_{T^*}}\right)S_{s_i}(\mathbf{x},t)\Delta t \tag{22}$$

For treating phase-change processes, one proposition of this paper is to re-scale the temperature values in relation to the saturation temperature of the fluid, $T^* = T - T_{sat}$. This modification facilitates the implementation of the interface conditions, as it is explained in Section 2.3. It is important to note that now the distribution functions are related to the variable T^* instead of T.

In the sequence, the equilibrium distribution functions are defined by Eq. (23), and the source term, by Eq. (24).

$$s_i^{eq} = w_i T^*\left[1 + \frac{\mathbf{c}_i\cdot\mathbf{u}}{c_s^2}\right] \tag{23}$$

$$S_{s_i} = w_i\left[\frac{\mathbf{c_i}\cdot\partial_t(T^*\mathbf{u})}{c_s^2} + T^*\dot{m}'''\left(\rho_g^{-1} - \rho_l^{-1}\right)\right] \tag{24}$$

By the same perturbation expansion mentioned before, the Chapman–Enskog analysis, from the thermal LBE it is possible to recover the energy conservation equation if $\alpha_l = c_s^2\left(\tau_T - 0.5\Delta t\right)$, where α_l is the liquid thermal diffusivity. The analysis mentioned here is presented in Appendix A.3 with more details.

To calculate the normalized temperature during the simulations, we use the zeroth moment of the temperature distribution functions, represented by Eq. (25).

$$T^* = \left[1 - \frac{\Delta t}{2}\dot{m}'''\left(\rho_g^{-1} - \rho_l^{-1}\right)\right]^{-1}\sum_{i=0}^{q-1} s_i \tag{25}$$

The vapor generation term is modeled similar to in Safari et al. [57]. However, as it is explained in Section 2.3, here we propose different methods for calculating the interface conditions, because the temperature profile closer to the interface has strong influence on $\dot{m}'''$ [87]. Then, the vapor source term is calculated by Eq. (26), where h_{lg} is the latent heat of vaporization, k_l is the liquid conductivity and K is a constant to be adjusted using the Stefan problem as calibration. The necessity of this constant is more clearly explained in Section 3 and it is due to the fact that the source term by itself has errors that not correctly capture the vapor generation rate.

$$\dot{m}''' = K\frac{k_l\nabla T^*\cdot\nabla\phi}{h_{lg}} \tag{26}$$

The temperature gradients away from the liquid–gas vapor interface are calculated using the traditional central finite difference scheme, Eq. (27), while the temporal derivative of $T^*\mathbf{u}$ is calculated using the backward scheme mentioned before, Eq. (28).

$$\nabla T^*(\mathbf{x}) = \sum_{i\neq 0}\frac{w_i\mathbf{c_i}T^*(\mathbf{x}+\mathbf{c_i}\Delta t)}{c_s^2\Delta t} \tag{27}$$

$$\partial_t\left(T^*\mathbf{u}\right)_{\mathbf{x},t} = \frac{3(T^*\mathbf{u})_{\mathbf{x},t} - 4(T^*\mathbf{u})_{\mathbf{x},t-\Delta t} + (T^*\mathbf{u})_{\mathbf{x},t-2\Delta t}}{2\Delta t} \tag{28}$$

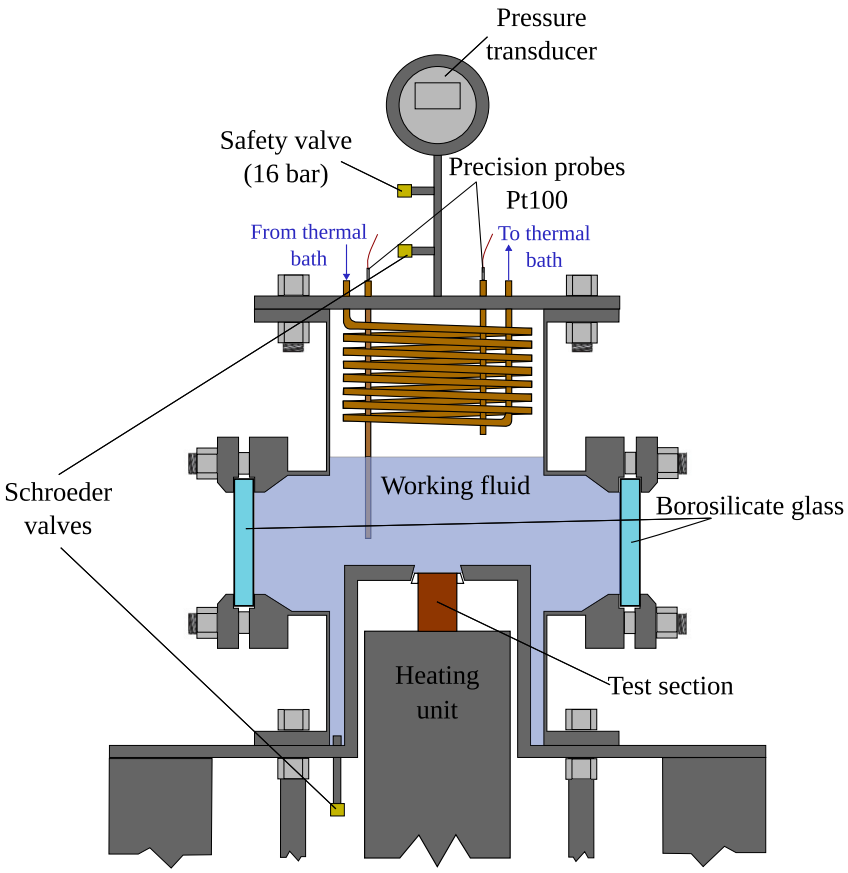

Fig. 1. Schematic diagram of the experimental facility used in this work.

2.3. Boundary and interface conditions

For the fluid flow modeling, three main kinds of boundary conditions (BC) were considered: rigid walls, fixed pressure and open boundaries.

The rigid walls were implemented through the bounce-back (BB) rule [88,89], which for both h_i and g_i can be represented by Eq. (29). In this equation, $*$ stands for the post-collision distribution functions, $\bar{i}$ the opposite direction of i and $\mathbf{x_b}$, the boundary location.

$$h_{\bar{i}}(\mathbf{x_b}, t+\Delta t) = h_i^*(\mathbf{x_b}, t); \qquad g_{\bar{i}}(\mathbf{x_b}, t+\Delta t) = g_i^*(\mathbf{x_b}, t) \tag{29}$$

For the fixed pressure BC, the bounce-back scheme was used for h_i, while the anti-bounce-back (ABB) rule from [90] was adapted for g_i, resulting in Eq. (30), where p_w is the fixed pressure at the outlet. With the anti-bounce-back condition we can guarantee the fixed pressure at the wall, which is not possible with the BB rule. Also, for convenience, the total pressure p is taken in relation to the saturation pressure, $p = P - P_{sat}$, where P is the absolute pressure. Then, the boundary pressure is set to $p_w = 0$, and the fluid is assumed to be stationary at the boundary ($\mathbf{u_w} = \mathbf{0}$), facilitating the implementation of this BC.

$$g_{\bar{i}}(\mathbf{x_b}, t+\Delta t) = -g_i^*(\mathbf{x_b}, t) + 2w_i \left\{ \frac{p_w}{c_s^2} + \rho_w \left[\frac{(\mathbf{c_i}\cdot\mathbf{u_w})^2}{2c_s^4} - \frac{\mathbf{u_w}\cdot\mathbf{u_w}}{2c_s^2} \right] \right\} \tag{30}$$

The open boundary was implemented by the extrapolation scheme [91] for the both distribution functions, as shown in Eq. (31). In this equation, $\mathbf{n}$ is the normal vector to the boundary, pointing into the domain.

$$h_i(\mathbf{x_b}, t+\Delta t) = h_i(\mathbf{x_b} - \mathbf{n}\Delta x, t+\Delta t); \qquad g_i(\mathbf{x_b}, t+\Delta t) = g_i(\mathbf{x_b} - \mathbf{n}\Delta x, t+\Delta t) \tag{31}$$

For the thermal LBM, it was considered also three kinds of BCs: adiabatic walls, fixed temperature walls and open boundaries. The first kind was implemented by the bounce-back rule considering zero heat flux: $s_{\bar{i}}(\mathbf{x_b}, t+\Delta t) = s_i^*(\mathbf{x_b}, t)$.

The walls with fixed temperature were implemented through the anti-bounce-back rule. For the temperature distribution functions, this condition can be given by Eq. (32), in which T_w^* is the fixed relative temperature at the wall.

$$s_{\bar{i}}(\mathbf{x_b}, t+\Delta t) = -s_i^*(\mathbf{x_b}, t) + 2w_i T_w^* \left[1 + \frac{(\mathbf{c_i}\cdot\mathbf{u_w})^2}{2c_s^4} - \frac{\mathbf{u_w}\cdot\mathbf{u_w}}{2c_s^2} \right] \tag{32}$$

At last, the open boundary was again implemented using the extrapolation scheme: $s_i(\mathbf{x_b}, t+\Delta t) = s_i(\mathbf{x_b} + \mathbf{n}\Delta x, t+\Delta t)$. Regarding that $\mathbf{n}$ is the normal direction pointing into the domain.

As mentioned before, here we propose a thermal boundary condition for the liquid–gas interface, in order to properly capture the temperature gradients close to the interface, which is very important for correctly capture the vapor-generation rate. As we assume that the vapor phase remains at saturation temperature, the anti-bounce-back rule, Eq. (32), can be used for implementing the fixed temperature at the interface $T_w = T_{sat} = 0$. If we use the absolute temperature, T, instead of the reference one, T^*, we must calculate the interface velocity $\mathbf{u_w}$ for implementing this BC, which is not a simple task. However, re-scaling the temperature in relation to the saturation temperature, we have $T_w^* = T_{sat}^* = 0$, and all the terms of Eq. (32) in braces vanish, resulting in $s_{\bar{i}}(\mathbf{x_b}, t+\Delta t) = -s_i^*(\mathbf{x_b}, t)$. This avoids the necessity of calculating the interface velocity, facilitating the implementation of the ABB rule at the interface and guaranteeing that the vapor remains at saturation temperature.

In addition, for modeling the wetting boundary condition at solid surfaces, we employed the model based on the minimization of the surface free energy, Ψ_s. Following the procedure proposed on Briant

et al. [42], the wetting condition at the solid–fluid interface can be expressed as follows,

$$\partial_{\phi}\Psi_s - \kappa \mathbf{n}\cdot\nabla\phi = 0. \tag{33}$$

According to de Gennes [92], Ψ_s can be approached by a power series of ϕ. Here we adopt the same cubic polynomial for the surface free energy as in Liang et al. [64]. Using the relation between the surface tensions and the contact angle from Young's law [93], from the free-energy minimization at the surface, being φ the equilibrium contact angle, we get the following equation for the contact boundary,

$$\mathbf{n}\cdot\nabla\phi = -\cos\varphi\left(\phi-\phi^2\right)\sqrt{\frac{2\beta}{\kappa}}. \tag{34}$$

Considering the link-wise approach for the boundary location in relation to the lattice centers [4], and supposing a south boundary in a 2D arrangement, the spatial derivative in the normal direction of Eq. (34) can be approached by $\partial_n\phi = \left(-8\phi_{x,w}/3 + 3\phi_{x,0} - \phi_{x,1}/3\right)/\Delta x$, where $\phi_{x,w}$ is the wall position, $\phi_{x,0}$ is the boundary node at $\Delta x/2$ distance from the wall and $\phi_{x,1}$ is the next node in the normal direction. Substituting this expression into Eq. (34) and defining $A = \Delta x\cos\varphi\sqrt{2\beta/\kappa}$, we get the following second order equation for determining the value of ϕ_w,

$$A\phi_{x,w}^2 + (8/3 - A)\,\phi_{x,w} + \left(\phi_{x,1}/3 - 3\phi_{x,0}\right) = 0. \tag{35}$$

The solution that remains between 0 and 1 is the value of ϕ_w at the boundary that guarantees the desired wettability, represented by the static contact angle φ. Then, the ghost nodes, $\phi_{x,-1}$, required for the calculation of Eqs. (17) and (18) can be calculated by extrapolation from the boundary node, $\phi_{x,0}$, and the wall node, $\phi_{x,w}$, as $\phi_{x,-1} = 2\phi_{x,w} - \phi_{x,0}$.

2.4. Experimental procedure

The bubble life-cycle features were also studied experimentally. A schematic view of the boiler setup is illustrated is in Fig. 1. The boiler chamber is a cylindrical vessel with two borosilicate windows at opposite sides, for the visualization of the boiling process. A JUMO pressure transducer is located at the top of the chamber, to measure the pressure inside the boiler. In addition, two precision Pt100 probes measured both liquid and vapor temperatures, to check that HFE-7100 fluid was operated under a saturated condition. More information about the experimental procedure can be seen in previous publications from the authors [71,72].

The test section shown in Fig. 2(a) was machined from a 60 mm diameter copper (Cu-Electrolytic Tough Pitch R300 – Cu> 99,9%) rod. Four T type thermocouples with a separation of five mm from each other were inserted in the axis of the test section to yield its temperature distribution. The temperature at the hot surface was determined through a linear fit with the temperature distribution inside the test section. Fig. 2(a) also illustrates the mirror-finishing of the hot surface at the top of the test section, in order to prevent from spurious bubbles. The mirror-finished surface in Fig. 2(a) is a circle of 30 mm diameter.

Five nucleation sites were manufactured with the help of a needle on the boiling surface of the test section (see Fig. 2(a)). We crafted more than one artificial site (five) in order to gain feasibility on the nucleation process. Fig. 2(b) is a picture recorded with a microscope of the company Dino-Lite with a RK-10-PX mounting device. It shows the particular nucleation site that effectively produced the set of bubbles (19) reported in this research. The site is about 120 μm diameter.

The procedure for measuring the bubble's characteristics is explained in Martins et al. [72], where the authors developed a model for determining the "mean bubble" and, then, the mean properties of its life-cycle. The mean bubble is a synthetic bubble that contains the average geometrical aspects (a 2D information about bubble width *per* height *per* time) of all bubbles measured in the experiments, with the uncertainties related to them. For more information about this technique, see Martins et al. [72]. This procedure yields the mean shape, equivalent radius (R_{eq}), apparent contact angle (φ_{ap}), dry radius (R_d), and forces acting on the typical bubble, and the corresponding uncertainty, which is of utmost importance for comparison of the experimental data with simulated results. The expressions adopted for calculating these forces can be seen in Appendix A.4. The referred mean bubble and mean properties were found from data for 19 bubbles obtained under the cited experimental operation conditions.

The bubble dry radius, R_d, is defined as the radius at the bottom of the bubble, close to the solid surface level. The bubble equivalent radius, R_{eq}, is calculated from the bubble volume, while the apparent contact angle, φ_{ap}, is the contact angle measured during the growth of the bubble. As mentioned before, all these variables are calculated using the mean bubble as reference. Thus, the resultant values of these properties represent the mean values found in all bubbles considered in the experiments.

3. Results

Both numerical and experimental results were obtained considering saturated HFE7100 as working fluid at $P_{sat} = 195$ kPa ($T_{sat} = 355.4$ K) and a superheating degree of $\Delta T = 5.1$ K. The thermodynamic and transport properties of the fluid at this condition were obtained from EES software [94], and are disposed in Table 1. For this operational condition the reduced pressure and temperature are $P_r = 0.087$ and $T_r = 0.758$, respectively.

The present phase-field model without phase-change was already validated by the simulation of two isothermal two-phase problems in Martins et al. [36]. In this previous work, there are solutions for the static bubble and the layered-Poiseuille flow problems for water–air and saturated water at different operational conditions.

For this paper, the codes were implemented in C language, using OpenMP parallel computing. The final simulations for the results showed here were executed in a workstation with 128 GB RAM DDR5, CPU AMD Threadripper 7980X with 64 cores (128 threads).

In the present paper we will develop the model validation in three stages: (i) the Stefan problem is solved to validate the model regarding the liquid–gas phase-change process, (ii) the contact-angle model will be tested for a wide range of static contact angles, in order to verify the accuracy on capturing the fluid–solid interaction, and (iii) the experimental evidence of a bubble life-cycle will be confronted with the numerical algorithm.

3.1. The Stefan problem

First, the model was employed for simulating the 1D liquid–gas Stefan problem. It consists of a one-dimensional liquid domain initially at saturation temperature, T_{sat}, that suddenly is submitted to a fixed wall temperature at the left boundary, $T_w = T_{sat} + \Delta T$, greater than the saturation temperature. This superheating evaporates the liquid, which is generated close to the left boundary. As the liquid is heated, more vapor is generated and the liquid–gas interface advances in x-direction with time. The right boundary is treated as an outlet boundary, thermally insulated with no velocity gradient ($\partial_x T = 0$ and $\partial_x u_x = 0$), being implemented with the equilibrium scheme, which assumes that the unknown functions are in equilibrium with the boundary velocity and density. The left boundary, a Dirichlet's kind of boundary, was implemented using the ABB scheme.

The Stefan problem has analytical solution and, thereby, it is usually employed for validating liquid–vapor phase-change models [23,95,96]. In our case, it will also be used for determining the vapor generation constant of Eq. (26), K, serving as a calibration test. This constant will be further used for the boiling simulation (Section 3.3). The analytical solution for the interface position, x_i, and the interface velocity, u_i,

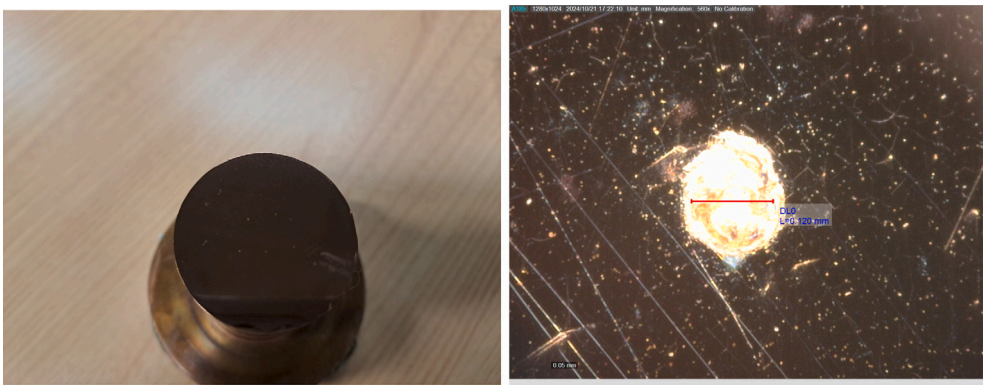

(a) (b)

Fig. 2. Top view of the copper probe body (a) and nucleation site manufactured with a needle (b).

Table 1
Properties of HFE7100 at saturation pressure of 195 kPa, used in all simulations.

	ρ (kg m^{-3})	μ (10^{-4}Pa s)	σ (10^{-3}N m^{-1})	k (10^{-2}W m^{-1} K^{-1})	c_p (J kg^{-1} K^{-1})	h_{lg} (J kg^{-1})	β_T (10^{-3}K^{-1})
Liquid	1355.718	3.145	7.742	5.764	1228.764	108 880.640	2.308
Vapor	18.091	0.212	–	0.979	974.052	–	–

with time, t, is given by Eq. (36), where $\alpha_g = k_g/(\rho_g c_{p,g})$ is the thermal diffusivity of the gas phase and ξ comes from the solution of Eq. (37).

$$x_i(t) = 2\xi\sqrt{\alpha_g t}$$
$$u_i(t) = \xi\sqrt{\frac{\alpha_g}{t}} \tag{36}$$

$$\xi e^{\xi^2}\,\mathrm{erf}(\xi) = \frac{c_{p,g}\Delta T}{h_{lg}\sqrt{\pi}} \tag{37}$$

It is important to mention that in this case we assume that there is only heat transfer in the gas phase, while the liquid phase remains at saturation temperature. This is the opposite of the previous hypotheses in Section 2.2. Also, the vapor generation term, Eq. (26), receives a minus signal. These changes are only made for this specific problem and, for any boiling-like problem, the assumptions and equations defined before remain, see Section 2.2.

For the simulations we used a domain of width $L = 1$ mm, employing a grid of 200 nodes with the D1Q3 velocity scheme. The spatial and temporal discrete intervals where $\Delta x = 5 \cdot 10^{-6}$ m and $\Delta t = 2.5 \cdot 10^{-7}$ s, with $W = 5\Delta x = 25$ μm and $M = 0.1\Delta x^2/\Delta t = 1.0 \cdot 10^{-5}$ m^{2}s^{-1}. These values lead to the following relaxation times: $\tau_{v,g} = 1.02 \cdot 10^{-6}$ s, $\tau_{v,l} = 5.0 \cdot 10^{-7}$ s, $\tau_{T^*} = 5.17 \cdot 10^{-7}$ s and $\tau_\phi = 8.0 \cdot 10^{-7}$ s. As the phase-field model presented here is not capable of generating vapor by itself, it is necessary to initialize an amount of vapor at the beginning of the simulation. This is because the method only drives the phase-change process after the existence of the two phases. Then, the initial condition for the simulation was $x_i = 0.15$ mm, with a linear temperature profile along x-direction, starting from T_w at $x = 0$ mm and ending with T_{sat} at $x = x_i = 0.15$ mm. The other variables where initialize with $p = p_{sat}$ and $u = 0$ m/s.

After the tests, we found that $K = 6.2$ was a good value, providing accurate results in comparison to the analytical solution, which can be verified in Fig. 3. In Fig. 3(a) we can realize the sensibility of the results to the value of K constant, as it is also presented the numerical solutions for $K = 7$, $K = 5$ and $K = 1$ (or without constant). An important remark to be clarify is that, in this calibration/validation test, we took careful to maintain the same values of Δx and Δt that was employed in the boiling simulation.

A grid analysis was performed in order to verify if the grid impacts on the constant choice, as well as, to see if the results are already converged. The solutions considering the previous grid and two other more refined grids can be seen in Fig. 4(a), and we can realize that the results are the same for the three different discretization levels. It is important to say that the interface width and the mobility value were kept the same value for all the simulations, $W = 25$ μm and $M = 1.0 \cdot 10^{-5}$ m^{2}s^{-1}. These results show that we can safely use the same grid in the forthcoming boiling simulations.

It is important to mention that, for this problem, the equilibrium scheme was employed instead of the extrapolation one because the last kind of BC creates some oscillations in the results. The equilibrium scheme neglects the non-equilibrium phenomena that may happen on the boundary [2]. Thus, we did a comparison between both BC schemes, which can be seen in Fig. 4(b). By the results, we can affirm that both BC schemes satisfactorily lead to very close results, confirming that the equilibrium BC can be used without preoccupations for this specific problem.

3.2. Contact angle model validation

The solid–fluid interaction between the bubble and the wall plays an important role guaranteeing the correct force balance during boiling, which reflects on the bubble detachment and its diameter at this stage. Thus, addressing the accuracy of the contact-angle implementation in the model becomes of huge importance.

As stated in Section 2.3, here we employed a free-energy-based model to insert the interaction between the liquid–gas interface and the solid wall. The input of this model is the equilibrium contact angle, φ, which represents the contact angle measured at equilibrium conditions.

For simulations, a droplet with radius of 0.15 mm is initialized over a surface with an initial angle of 90°. Then, the simulation is carried out until the bubble reaches equilibrium (i.e., stops moving). The contact angle is, then, measured and compared with the expected one (the equilibrium contact angle used as input). In this case, for measuring the resultant contact angle from simulations we used the ImageJ software with the DropSnake plug-in [97], applying the procedure to the density profile figures.

We employed $\Delta x = 5 \cdot 10^{-6}$ m and $\Delta t = 2.5 \cdot 10^{-7}$ s, using a grid of 300:200 lattices and an interface width of $W = 5\Delta x = 25$ μm. All the properties of the HFE7100 were employed here (see Table 1), with their respective relaxation times.

The results are depicted in Fig. 5, where we can see a good agreement between the expected contact angle and the measured from the simulations. Only for values below 15° or above 145° the results start

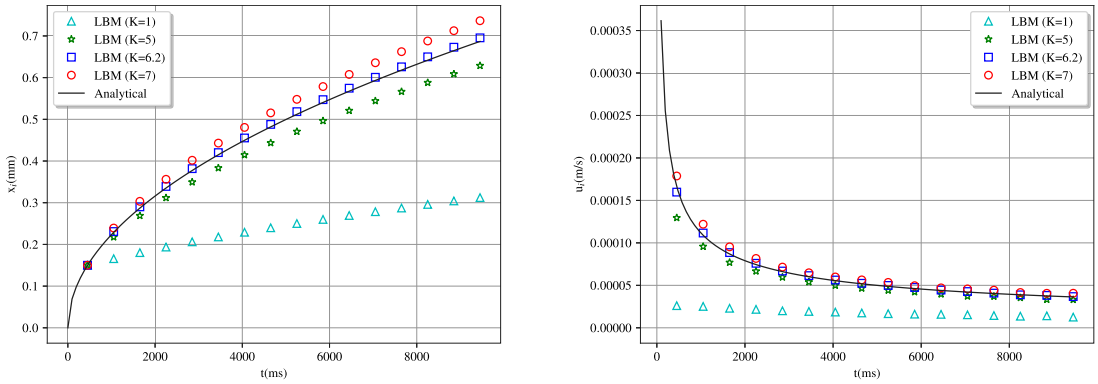

Fig. 3. Liquid–gas interface position (a) and interface velocity (b) with time for the Stefan problem, considering different values for K in comparison to the analytical solution.

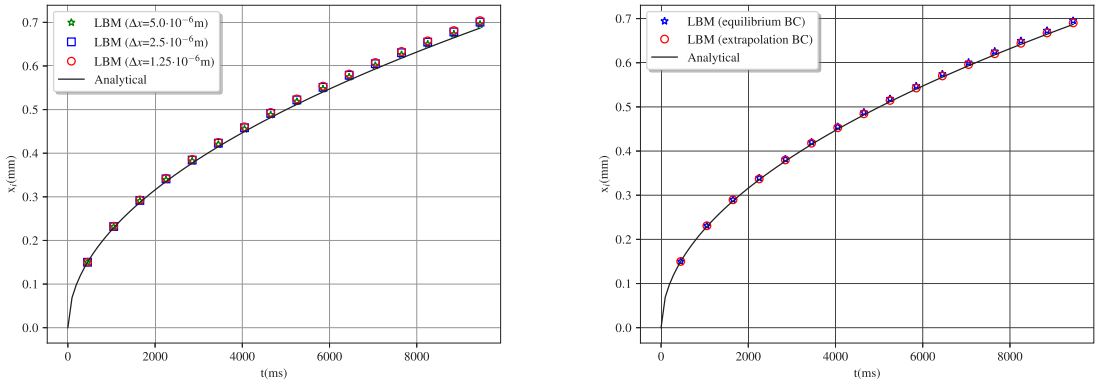

Fig. 4. Grid analysis of the Stefan problem considering 3 grid levels (a) and Difference between extrapolation and equilibrium BC schemes (b).

to deviate more significantly from the input φ value. Therefore, as the static contact angle between the HFE7100 and the polish coper surface is about 6°, it is expected some deviations or challenges during the boiling simulation, which are debated in the next section. The errors for φ >150° have already been reported by other authors from the literature [56,64]. However, usually the simulations did not use the full set of physical properties of real fluids, such as the HFE7100, which has considerable high viscosity and density rations between the gas and liquid phases, as well as, higher surface tension than the common value adopted in the literature. Thus, the significant deviations yielded for $\varphi < 15^o$ can be related to effects from the considerable high density (75) and kinematic viscosity (15) ratios, as well as high surface tension value, see Table 1.

3.3. Single bubble life-cycle under pool boiling

The operational conditions and the properties of the HFE7100 are reported in Table 1. Simulations were developed in a rectangular domain with dimensions of 6 and 7 mm in width and high, respectively. The upper part of the domain was considered as saturated vapor, whereas the bottom is saturated liquid. The interface between gas and liquid phases was placed 3 mm below the uppermost limit of the domain. An additional effort was made to properly reproduce a nucleation site, somehow, similar to that manufactured in the experiments. Accordingly, a V shape cavity was placed in the middle of the bottom wall. The radius of the simulated is R_c = 0.06 mm, which is similar to the experimental one, as shown in Fig. 2(b). The numerical site was designed with 45° of inclination in relation to the horizontal. Previous numerical features are illustrated in Fig. 6.

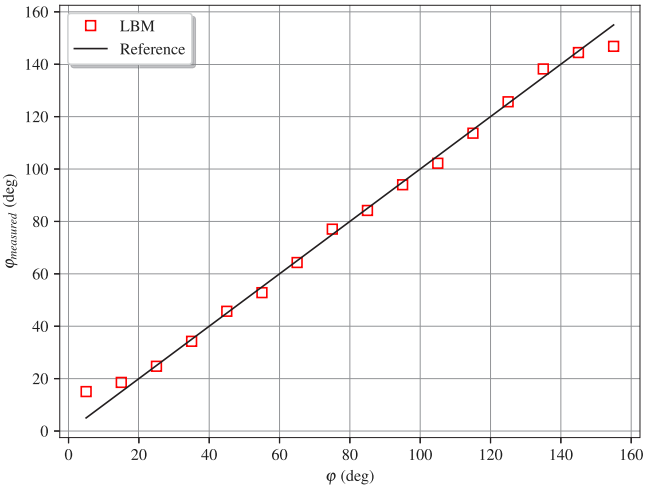

Fig. 5. Validation of the contact-angle model for a static droplet.

The lateral and bottom walls are assumed to be rigid, implemented using the bounce-back scheme for both distribution functions, h_i and g_i. The top wall remains at a constant pressure of P_{sat}, which is imposed by the anti-bounce-back scheme for g_i, Eq. (30), and the bounce-back scheme for h_i, Eq. (29). At the bottom wall, the contact-angle model is employed for considering the wetting phenomena between the fluid and the solid.

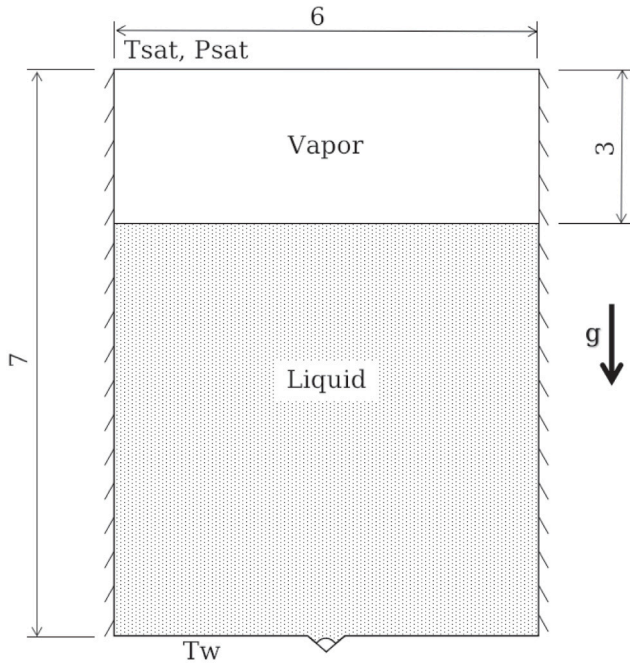

Fig. 6. Scheme of the computational domain simulated, dimensions in mm.

Regarding the thermal boundary conditions, the bottom wall is assumed to be at a constant superheated temperature T_w, and the top, at T_{sat}. Both are implemented using the anti-bounce-back scheme for s_i, Eq. (32). The lateral walls are considered as adiabatic, being modeled by the bounce-back rule as explained in Section 2.3.

The domain was initialized in equilibrium, i.e. $h_i = h_i^{eq}$, $g_i = g_i^{eq}$ and $s_i = s_i^{eq}$. The pressure and the velocity fields were initialized uniform at P_{sat} ($p = 0$) and $\mathbf{u} = \mathbf{0}$. For the initial density profile, we considered a vapor layer with 3 mm width at the top of the domain and a small bubble of radius $R_{ini} = 10\Delta x$ at the bottom center of the cavity, as represented in Fig. 6. All the interfaces between phases were initialized considering the hyperbolic tangential profile given by Eq. (20).

For the initial temperature profile, all the domain was assumed to be at saturation temperature, T_{sat}, except for the lattices near to the bottom wall. In this region, a thermal boundary layer of width δ_{ini} with a linear profile between T_w and T_{sat} was considered. Recall we are trying to numerically simulate the experiments inside a real boiling chamber. Throughout the experiments the nucleation site was already active, this situation was kept when the data was collected and, for sure, this feature affected the thermal boundary layer. As a result, is seems pertinent to use a boundary layer correlation specifically reported for this condition. Accordingly, we choose the correlation given by Han and Griffith [98], represented by Eq. (38).

$$\delta_{ini} = \frac{3}{2}\frac{\Delta T R_c}{T_w - T_{sat}\left(1 - \frac{2\sigma}{R_c \rho_g h_{lg}}\right)} \tag{38}$$

The discrete time and space intervals were $\Delta x = 5.0 \cdot 10^{-6}$ m and $\Delta t = 2.5 \cdot 10^{-7}$ s. The interface width was $W = 5\Delta x = 25$ μm and the values of the relaxation rates for $\boldsymbol{\Lambda}$, τ_T and τ_ϕ are calculated directly using the properties of the fluid (Table 1) and the values of Δx and Δt. Again, it is important to effort that all the real properties of the HFE7100 were employed on the LBM simulation, using directly physical units without the necessity of employing lattice units, as reported in Martins et al. [36].

Given HFE7100 volatility, and mainly its high wettability, the experimental contact angle determination of HFE7100 in polished copper is not straight forward [71,72]. According to previous references, the expected static contact angle is almost null, even though in the first stages of the drop deposition could be considered at about 6°. Recall the numerical solver requires the input of a static contact angle to develop the simulations. Indeed, its value becomes of great importance, since it will affect the dynamics of the bubble, mainly, at the final stage of the bubble life-cycle.

Numerical simulations will show that the dry radius of the bubble is almost coincident with the size of the manufactured nucleation site at the experimental test section, reported in Fig. 2(b). Moreover, this particular feature takes place throughout almost the whole life-cycle of the bubble. The maximum value of the dry radius for the experimental results is about 0.07 mm, which is only slightly above the size of the manufactured site, which is about 0.06 mm. In the case of the numerical results, the maximum value of R_d is about 0.055 mm. As this peculiar feature takes place for both numerical and experimental results, it seems there is a close relationship between the site and the dry radius of the bubble, at least for the operating conditions reported herein. Given that the triple line is located within the region affected by the nucleation site, it seems more than questionable that the proper static contact angle is the one provided by the polished surface. Thus, we choose a value of static contact angle that would give a bubble period near to the experimental one.

It is important to realize that the static contact angle is the only input to our model that really depends on the experimental results. All other parameters are physical properties of the fluid. Also, given the uncertainty of the real value of the static contact angle in the cavity, this choice based on the experimental results is justified. In the end, the value of 16.73^o was used as input for the wetting model. This angle provided a numerical bubble period of 54 ms, while the experimental period was 53 ms.

The results for density fields and streamlines in the liquid phase can be seen in Fig. 7. By the streamlines we can see that the bubble expansion provokes an upward movement on the fluid. Also, some downward lines can be seen, mainly in Fig. 7(b), due to the fluid that is replacing the portion accelerated and consumed by the growth of the bubble. These results illustrate the capability of the model to capture the movement induced by the bubble growth.

A qualitative comparison between the numerical bubble and one of the recorded experimental bubbles can be seen in Fig. 7. By this figure, we realize that the simulated and experimental shapes are very similar, reinforcing the applicability of the proposed simulation procedure. However, after the detachment of the bubble, there are more differences between the numerical and experimental results. This can be due to, first, a second bubble pushing the detached bubble away from the surface and, second, oscillations at the bulk fluid in the experiments. As bubbles are very small compared to the boiling vessel, they are easily moved by the liquid currents surrounding them. In the case of the numerical simulations, after the bubble's detachment we do not have a second bubble growing in the cavity. This is because we are simulating one bubble cycle only, considering that the phase field LBM needs an initial seed and, for a second cycle, an other nucleus would have to be inserted.

For a quantitative verification, we directly compare the shapes of the numerical bubble with the mean shape of the experimental bubbles, which can be seen in Fig. 9. This comparison allows us to truly evaluate the accuracy of the method when capturing bubble's characteristics. It confirms that, at the initial stages, there are more significant deviations between the numerical and the experimental results than in the final growth stage. Even so, the data provided by the LBM show a very good accuracy in predicting the bubble's shape, evidencing a good capability of dealing with single bubbles under pool boiling. In fact, considering all results from Fig. 9, the highest absolute error between the experimental and numerical results is approximately equal to 0.05 mm in y value.

Here it is important to clarify that, for the calculation of R_{eq}, V, R_d and φ_{ap}, the reference line was taken coincident with the plane wall at

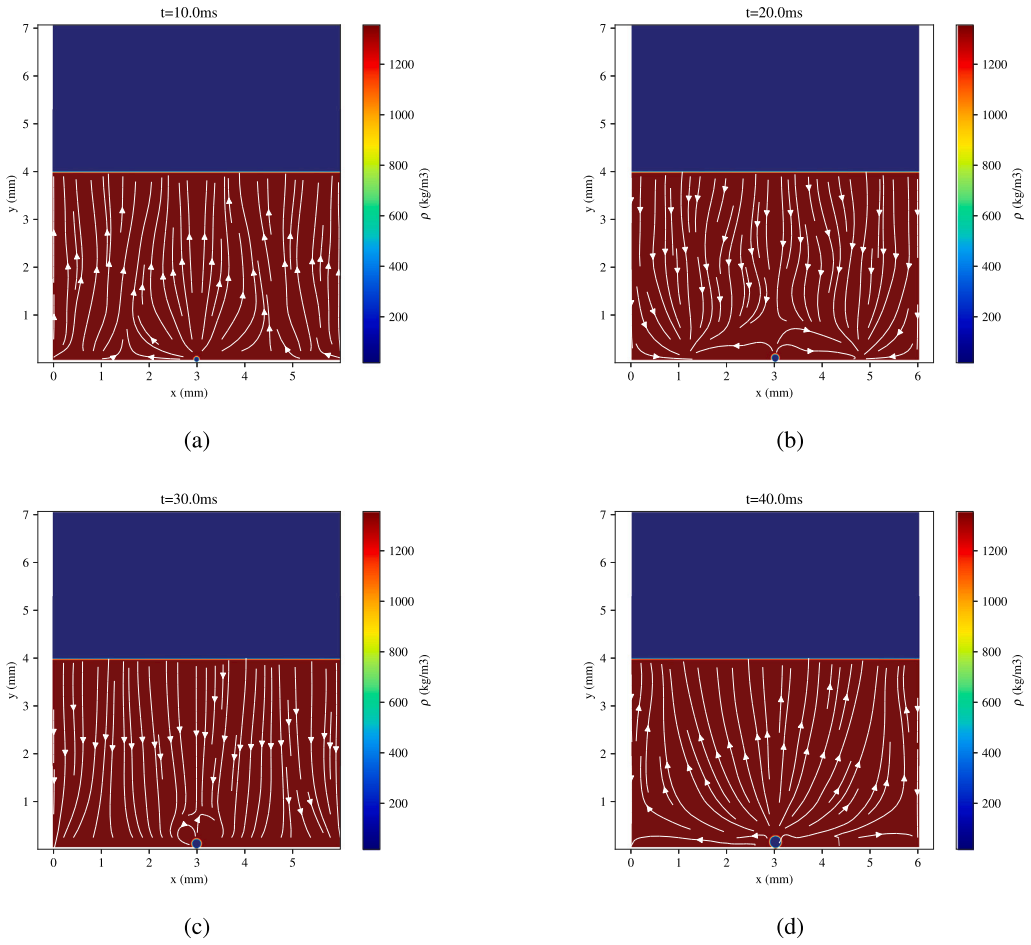

Fig. 7. Density contours with streamlines in the liquid from LBM simulations.

the bottom of the domain, just above the cavity. This choice was made to provide a fair comparison between the numerical and experimental results, because in the experiments the reference line for the bottom of the bubble was also taken as the horizontal plane, just above the cavity. Then, despite an initial bubble of radius $10\Delta x$ being placed at the beginning of the simulation, it remains entirely inside the cavity (below the horizontal plane wall). Consequently, in the graphics of R_{eq}, V, R_d and φ_{ap} and in the numerical representation of the bubble (Figs. 8 and 9), this initial radius does not appear.

Also, for the determination of the apparent contact angle, a different procedure than used in Section 3.2 was employed. In order to make a fair comparison between numerical and experimental results, we used the same methodology than in Martins et al. [72] for the determination of φ_{ap}, which is the secant method. This method considers two points along the contact line of the bubble: one at the triple point, close to the wall, and other at the interface in an arbitrary distance of the wall. This distance was chosen the same than for measuring the experiments, 30 μm.

Treating of geometric aspects of the bubble, we compare the equivalent radius, the bubble volume, the dry radius and the apparent contact angle of the numerical bubble with the experimental data. As we can see in Fig. 10 and in Fig. 11, the great part of the numerical data remains within the uncertainty of the experimental results. This fact confirms again the precision of the proposed LBM for capturing the geometrical aspects of the bubble life-cycle. The tendency of the curves also corresponds to that of the experimental data, showing the physical coherence and accuracy of the simulations. Only the apparent contact angle curve deviates from the experiments. However, this fact can be connected to structures present in the test-section cavity that are not considered in the simulations, where a smooth 45° cavity is considered. Then, a continuous decrease of φ_{ap} is expected in the numerical results as a consequence of the smooth surface. In the case of the experiments, there is the possibility of having structures that retain the bubble at a constant apparent contact angle, which is observed in Fig. 11(a).

It should also be observed that the bubble detaches without almost showing a decrease in the growing velocity, which seems to be almost constant at the end of the growth period. It is only at the end of the curves that this tendency starts to deviate more, besides the results getting closer to the experimental ones. This fact may be due to the absence of a second bubble nucleating in the V cavity. For the phase-field LBM, the nucleation site remains active only for static contact angles above 90° for flat walls, or above the cavity angle for V-shaped cavities, see Begmohammadi et al. [59], Sadeghi et al. [60]. As the static contact angle for the HFE7100 in a copper surface is low (below 45°, which is the V-cavity angle), the nucleation site does not remains active. So we do not see a new bubble pushing the detached bubble upward, a behavior that would be expected in real conditions. Without this second bubble, the fluid inundates the cavity and more vapor is generated at the bottom part of the bubble, changing the derivative of R_{eq} curve at 37 ms. This would be avoided if there was a new bubble at the nucleation site. Thus, for the next steps of our research, it would be interesting to develop a nucleation model for the LBM proposed here. Besides this fact, the accuracy of the method is still very good.

Now, for a evaluation of the dynamics present in the phenomena, we calculate the forces acting on the bubble during its growth. The main forces are the contact pressure force, F_{cp}, the surface tension force, F_σ, the buoyancy force, F_b, and the dynamic force, F_D. The calculation of these forces can be seen in Appendix A.4.

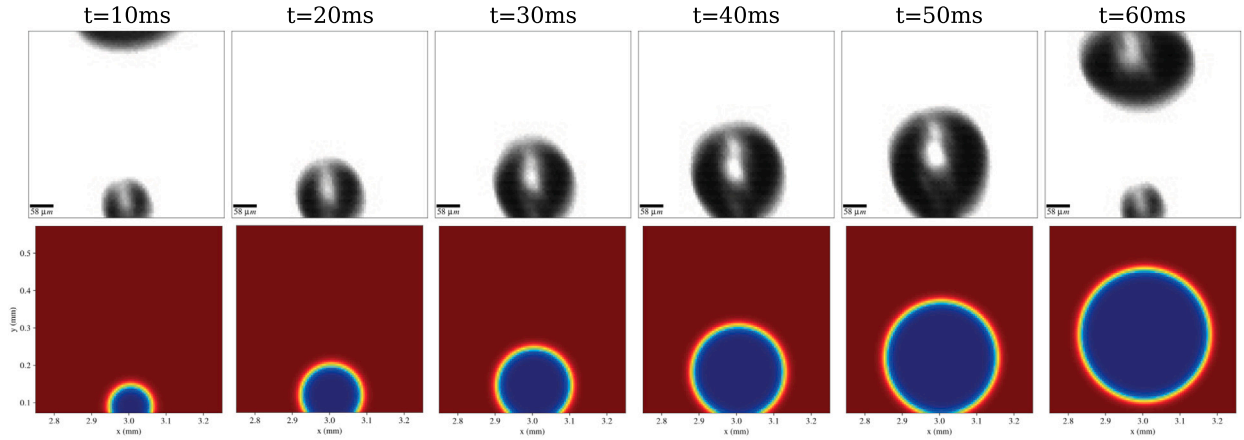

Fig. 8. Transient snapshot of one particular experimental bubble and the corresponding LBM results.

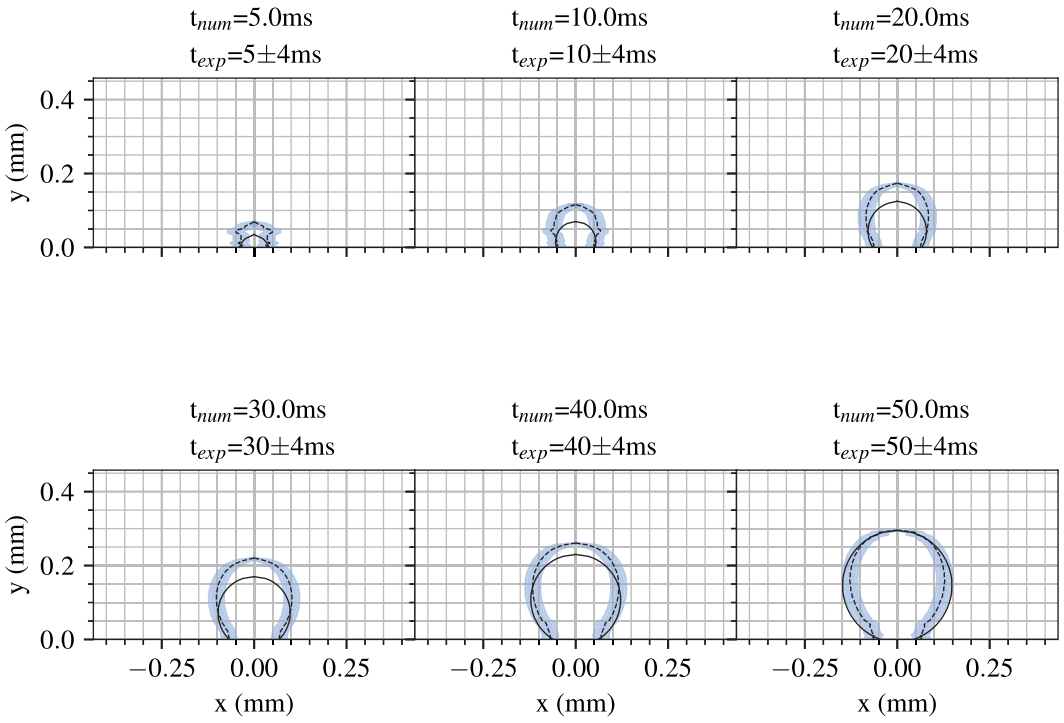

Fig. 9. Comparison between mean bubble profile from experiments and from LBM. The solid lines are the LBM results, while the dashed lines are the experimental results with the uncertainties in blue.

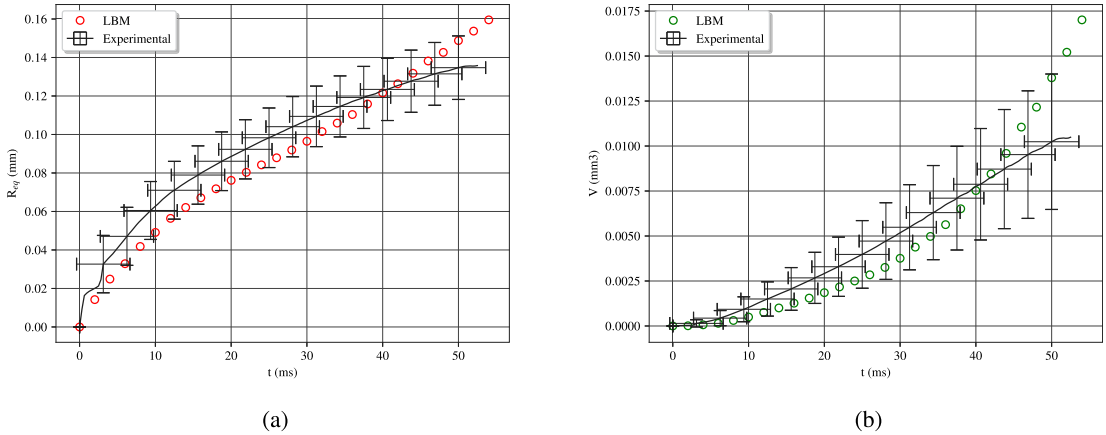

Fig. 10. Comparison between equivalent radius (a) and bubble's volume (b) from experiments and from LBM.

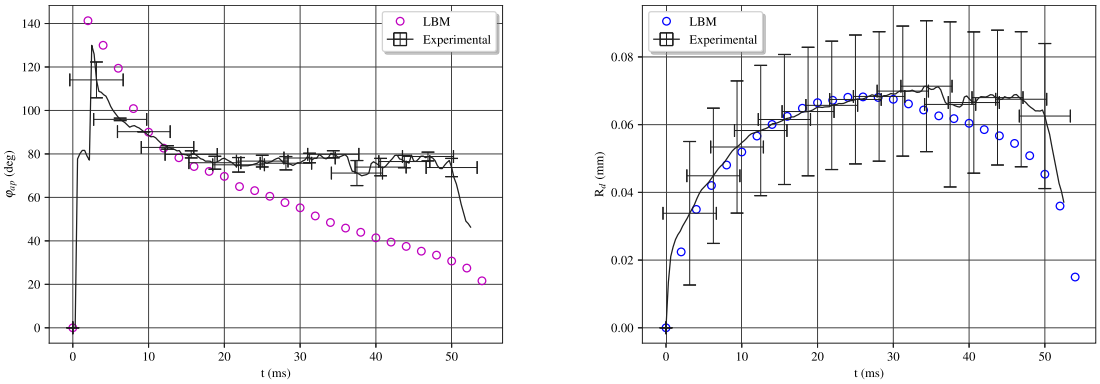

Fig. 11. Comparison between apparent contact angle (a) and dry radius (b) from experiments and from LBM.

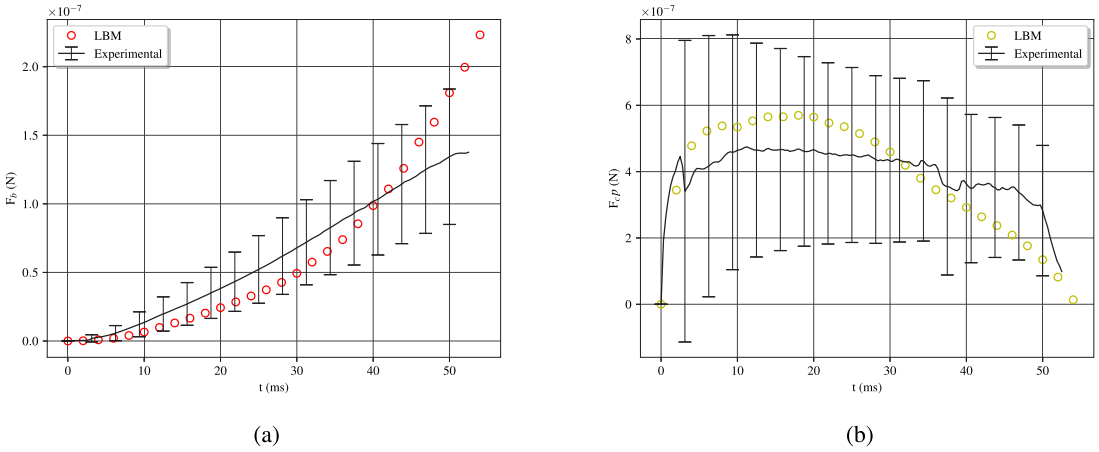

Fig. 12. Comparison between buoyancy (a) and contact pressure forces (b) from experiments and from LBM.

Table 2
Relative errors of the numerical simulations in comparison to the experimental data.

	R_{eq}	V	R_d	φ_{ap}	F_b	F_{cp}	F_D	F_σ
E_{L1} (%)	11	26	9	30	26	21	30	25

The buoyancy force, which depends mainly on the bubble volume, is depicted in Fig. 12(a). We can see that the numerical results remain almost always inside the uncertainty bar of the experimental results, similarly to the bubble volume, as expected. Next, the contact pressure is reported in Fig. 12(b). In this case, the numerical and experimental results are closer to each other in comparison to the other forces. Meanwhile, in Fig. 13(a) we have the surface tension force, the only force keeping the bubble attached to the wall in this case. At last, in Fig. 13(b) we have the dynamic force, that accomplishes for both lift and unsteady growth effects.

Once more, the results from LBM are very accurate in comparison to the experimental data, as the great part of the simulated results remain inside the uncertainty of the experimental results. This reaffirms the capability of the present model of correct simulating the dynamic behavior of a single bubble under pool boiling. It should be noted that the force values are very low, being of the order of 10^{-6} and 10^{-7}, meaning that the numerical model is very accurate in its quantitative predictions.

$$E_{L1} = 100\frac{\sum_{n=0}^{N} |\chi_n^{LBM} - \chi_n^{exp}|}{\sum_{n=0}^{N} |\chi_n^{exp}|} \tag{39}$$

The relative errors for the numerical results in comparison to the experimental data are disposed in Table 2, considering the L1 norm — see Eq. (39). Analyzing Table 2, we can see that they remain between 10% and 30%. Therefore, besides having "high" values for some variables, almost all the trends of the numerical curves match those measured from experiments, excepting the contact angle, a topic already discussed before.

In addition, the relative errors do not give a good estimative of how really close the numerical results are to the experimental data. In fact, a graphical comparison of the figures shows that almost all numerical curves stay inside the uncertainty region of the experimental data. It is important to evidence that this quantitative comparison with experimental results is rare in the LBM community, especially considering the model proposed here, which directly uses all physical properties of the fluid under real operational conditions.

Another important topic to be mentioned is that in this work we restricted ourselves to a two-dimensional description of the boiling phenomena, as the main objective was to propose and validate a new phase-field LBM model to simulate the liquid–gas phase-change process. However, approaching a 3D phenomena using a 2D model can have issues, because some effects of three-dimensional curvatures are not included in the analysis.

As observed in Table 2, the forces and the bubble volume were the variables with higher errors. This can be connected to the fact that these variables are the ones with stronger dependency of 3D features, and to calculate them here we used a 2D approach and, then, we needed to make assumptions about the two-dimensionalization of a 3D bubble. Thus, future studies regarding the expansion of the present model to 3D are of great importance.

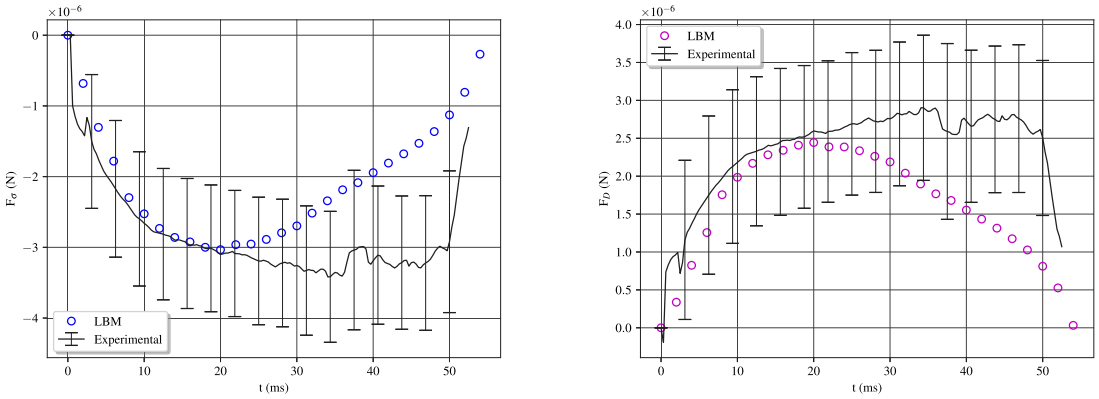

Fig. 13. Comparison between surface tension (a) and dynamic forces (b) from experiments and from LBM.

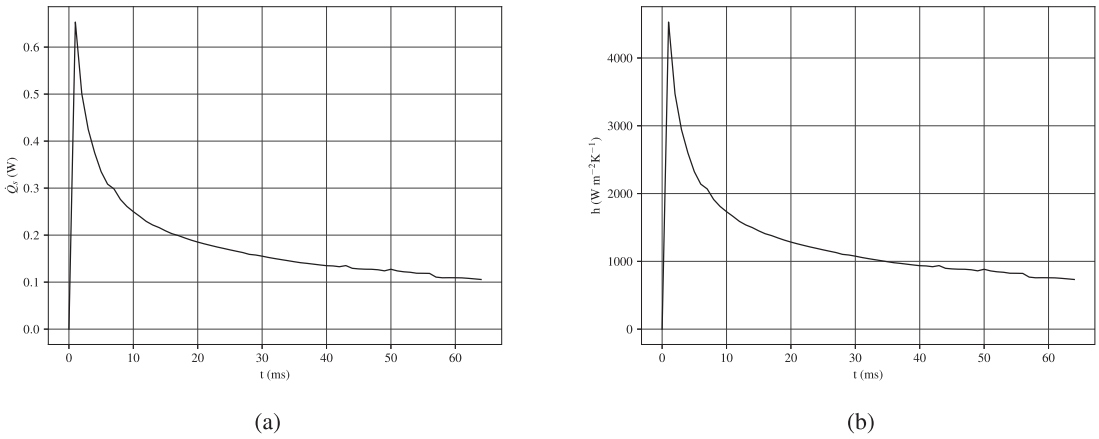

Fig. 14. (a) Heat transfer rate at the surface with time and (b) mean heat transfer coefficient at the surface with time for the numerical simulation.

At last, the detailed results provided by the numerical simulations also allow the calculation of the total heat transfer rate emanating from the superheated surface. As for the bubble volume calculation, we assume that each width of the bubble per y is a cylindrical disk, to estimate the heat transfer rate at the surface we also assumed that it is a circular disk with a diameter L. Then, using Fourier's law to calculate the heat flux, considering only the wet zone of the bottom wall (regions insulated by the vapor are neglected), and taking the mean heat flux between the cells of the bottom wall, we achieve the Eq. (40). In this equation, the derivative in y direction was approached by a second order forward finite difference scheme, and j represents the nodes in x direction, while N_x, the total number of nodes in x direction.

$$\begin{aligned}\dot{Q}_s(t) &= \pi\frac{L^2}{4}\overline{\dot{q}''}(t) = \pi\frac{L^2}{4}\frac{1}{L}\int_0^L -k_l\frac{\partial T}{\partial y}(t,x,y=0)\,dx \\ &\approx \frac{-k_l\pi L_x}{4}\sum_{j=0}^{Nx}\frac{-T_{j,2}(t)+4T_{j,1}(t)-3T_{j,0}(t)}{2}\end{aligned} \tag{40}$$

The heat transfer rate can be seen in Fig. 14(a). As the superheating degree is constant in the case studied, $\Delta T = 5.1K$, using Newton's law of cooling we can also determinate the mean heat transfer coefficient (HTC) at the surface, $\overline{h} = \overline{\dot{q}''}/\Delta T$, which is shown in Fig. 14(b). The behavior of $\overline{h}$ is as expected, because as the bubble grows, the area insulated by the vapor at the superheated wall increases. Consequently, decreasing the heat transfer rate of the surface, until the bubble detaches, at $t = 54$ ms. It is important to mention that, for both $\dot{Q}_s$ and $\overline{h}$, there are no experimental results for comparison because we did not have measurements of the heat flux close to the surface.

The results shown in this section demonstrate the accuracy of the proposed method in capturing the features of a single bubble under pool boiling. Beyond this fact, the simulations are carried out using the full set of real properties of the HFE7100 and they are implemented directly using physical units. These are a remarkable novelty for the LBM community and allowed the validation of the method. Also, the experimental data provided here can be used as a benchmark test for other authors, considering a high saturation pressure operational condition. Note this research makes available the experimental data as supplementary material. Hopefully, these data will provide numerical scientists useful information to test the performance of their numerical models. The downloadable file is structured in the same fashion as reported in Martins et al. [72].

4. Conclusions

This work reported a LBM for boiling simulation where the use of lattice units are no longer necessary. The entire simulation was performed in physical units. As a result, the physical properties of the fluid are imposed in a natural manner. The model was calibrated and validated with both analytical and experimental evidence.

In a first step, the calibration term for the vapor generation was performed in the basis of the Stefan problem. The calibration was only related to the operational condition: fluid, pressure, temperature, and superheating degree. After the calibration, the model yielded negligible errors. In a second step, the static contact angle model imposed to the model was tested in order to evaluate the ability of the method

on recovering the proper interphase in the near vicinity of the triple line. The model showed an outstanding performance for static contact angles between 15° and 150°. More research is needed to improve the numerical model for very low and very high contact angles.

In a third (and final) step, a single bubble of saturated HFE7100 under pool boiling was simulated. Besides, this research reports the experimental test that matches the operational condition of the numerical study. The typical experimental bubble was yielded from the life-cycle of 19 bubbles. The experimental uncertainties provided an useful reference for the assessment of the numerical results. The operating conditions in terms of reduced pressure and temperature were 0.087 and 0.758, respectively. Both sets of results were confronted with a notable degree of success.

The experimental analysis allowed for comparison of the bubble shape with time, geometrical aspects of the bubble life-cycle (equivalent radius, bubble volume, dry radius and apparent contact angle) and also the set of forces acting on the bubble. Numerical results showed a very good agreement with the experimental data, remaining inside the uncertainty of the experiments for almost the whole life-cycle of the bubble. This fact evidences the capability of the method on capturing the boiling phenomena, considering both geometrical and dynamical aspects.

In addition, this work provides detailed experimental information on a single bubble of saturated HFE7100 under pool boiling. This information is freely available as supplementary material, and its is formatted in the manner described in Martins et al. [72]. This set of data can serve as a benchmark exercise for numerical scientists interested in validating their models.

Then, the main conclusions of this work can be summarized in the following points:

- A new phase-field LBM for liquid–gas phase-change simulation, which allows the direct use of physical units, was successfully proposed.
- The new methodology was validated first with theoretical problems and, then, with experimental results, showing a good accuracy and applicability.
- The results suggested that a deep study regarding the contact angle model needs to be performed in the future.
- This paper also provided valuable experimental information about the life-cycle of a single bubble of HFE7100 under saturation conditions of P_{sat} = 195 kPa, which can be used as benchmark for further numerical studies.

CRediT authorship contribution statement

Ivan Talão Martins: Writing – review & editing, Writing – original draft, Visualization, Validation, Software, Methodology, Investigation, Formal analysis, Data curation, Conceptualization. **Luben Cabezas Gómez:** Writing – review & editing, Writing – original draft, Visualization, Validation, Supervision, Resources, Project administration, Methodology, Investigation, Funding acquisition, Formal analysis, Data curation, Conceptualization. **Pablo Fariñas Alvariño:** Writing – review & editing, Writing – original draft, Visualization, Validation, Supervision, Resources, Project administration, Methodology, Investigation, Funding acquisition, Formal analysis, Data curation, Conceptualization.

Declaration of competing interest

The authors declare that they have no known competing financial interests or personal relationships that could have appeared to influence the work reported in this paper.

Acknowledgments

The authors acknowledge the support received from FAPESP, Brazil (São Paulo Research Foundation, grants 2022/15765-1 and 2023/02383-6) and CNPq, Brazil (National Council for Scientific and Technological Development, process 305771/2023-0), and the funding for 1g. This work used resources of the "Centro Nacional de Processamento de Alto Desempenho em São Paulo (CENAPAD-SP)".

Appendix. Chapman–Enskog analysis

In this section, the Chapman–Enskog procedure for recovering the macroscopic conservation laws is presented for each LBE. The subindex α, β and γ will be used for representing the Cartesian coordinates in the Einstein notation.

A.1. Allen–Cahn equation

Starting by Eq. (3), the aim is tho recover the full Allen–Cahn equation, Eq. (2). First, we need to determine the moments of the equilibrium distribution function, Eq. (4), and the source term, Eq. (7):

$$\begin{cases} \sum_i h_i^{eq} = \phi; \\ \sum_i c_{i\alpha} h_i^{eq} = \phi u_\alpha; \\ \sum_i c_{i\alpha} c_{i\beta} h_i^{eq} = c_s^2 \phi \delta_{\alpha\beta}. \end{cases} \tag{41}$$

$$\begin{cases} \sum_i S_{h_i} = -\frac{\dot{m}'''}{\rho_l}; \\ \sum_i c_{i\alpha} S_{h_i} = \partial_t \left(\phi u_\alpha\right) + c_s^2 \lambda n_\alpha. \end{cases} \tag{42}$$

Starting from the LBE for the Allen–Cahn equation, Eq. (3), we first expand $h_i(x_\alpha + c_{i\alpha}\Delta t, t + \Delta t)$ in Taylor series. Then, we substitute into the LBE, considering terms only up to second order:

$$\Delta t \left(\partial_t + c_{i\alpha}\partial_\alpha\right) h_i + \frac{\Delta t^2}{2}\left(\partial_{tt} + 2c_{i\alpha}\partial_{t\alpha} + c_{i\alpha}^2 \partial_{\alpha\alpha}\right) h_i = -\frac{\Delta t}{\tau_\phi}\left(h_i - h_i^{eq}\right) + \Delta t S_{h_i}. \tag{43}$$

Next, we expand the derivatives, the distribution functions and the source term in terms of the Knundsen number, represented by ϵ:

$$\begin{cases} h_i = h_i^{(0)} + \epsilon h_i^{(1)} + \epsilon^2 h_i^{(2)}; \\ \partial_t = \epsilon \partial_t^{(1)} + \epsilon^2 \partial_t^{(2)}; \\ \partial_\alpha = \epsilon \partial_\alpha^{(1)}; \\ S_{h_i} = \epsilon S_{h_i}^{(1)}. \end{cases} \tag{44}$$

Substituting into Eq. (43) and neglecting terms with order superior than ϵ^3, we have:

$$\begin{aligned} &\epsilon^0 \left[\frac{1}{\tau_\phi}\left(h_i^{(0)} - h_i^{eq}\right)\right] + \epsilon^1 \left[\partial_t^{(1)} h_i^{(0)} + c_{i\alpha}\partial_\alpha^{(1)} h_i^{(0)} + \frac{h_i^{(1)}}{\tau_\phi} \right. \\ &\left. - \left(1 - \frac{\Delta t}{2\tau_\phi}\right) S_{h_i}^{(1)}\right] + \cdots \\ &\epsilon^2 \left[\partial_t^{(1)} h_i^{(1)} + \partial_t^{(2)} h_i^{(0)} + c_{i\alpha}\partial_\alpha^{(1)} h_i^{(1)} + \frac{\Delta t}{2}\left(\partial_t^{(1)} + c_{i\alpha}\partial_\alpha^{(1)}\right)^2 h_i^{(0)} \right. \\ &\left. + \frac{h_i^{(2)}}{\tau_\phi}\right] = 0 \end{aligned} \tag{45}$$

Separating the scales of Eq. (45), considering the same order of ϵ:

$$\epsilon^0 : h_i^{(0)} = h_i^{eq}; \tag{46}$$

$$\epsilon^1 : \left(\partial_t^{(1)} + c_{i\alpha}\partial_\alpha^{(1)}\right) h_i^{(0)} = -\frac{h_i^{(1)}}{\tau_\phi} + \left(1 - \frac{\Delta t}{2\tau_\phi}\right) S_{h_i}^{(1)}; \tag{47}$$

$$\epsilon^2 : \partial_t^{(2)} h_i^{(0)} + \left(\partial_t^{(1)} + c_{i\alpha}\partial_\alpha^{(1)}\right) h_i^{(1)} + \frac{\Delta t}{2}\left(\partial_t^{(1)} + c_{i\alpha}\partial_\alpha^{(1)}\right)^2 h_i^{(0)} = -\frac{h_i^{(2)}}{\tau_\phi}. \tag{48}$$

If we substitute Eq. (47) into Eq. (48), we have:

$$\partial_t^{(2)} h_i^{(0)} + \left(\partial_t^{(1)} + c_{i\alpha}\partial_\alpha^{(1)}\right)\left(1 - \frac{\Delta t}{2\tau_\phi}\right) h_i^{(1)} = -\frac{h_i^{(2)}}{\tau_\phi} - \frac{\Delta t}{2}\left(\partial_t^{(1)} + c_{i\alpha}\partial_\alpha^{(1)}\right) \times \left(1 - \frac{\Delta t}{2\tau_\phi}\right) S_{h_i}^{(1)}. \tag{49}$$

By Eq. (8), Eq. (41) and (42), we see that $\sum_i h_i = \sum_i h_i^{eq} - \Delta t/2 \sum_i S_{h_i}$. Expanding in terms of ϵ, we have $\sum_i h_i^{(1)} = -\Delta t/2 \sum_i S_{h_i}^{(1)}$ and $\sum_i h_i^{(2)} = 0$.

Taking the zeroth and the first moments of Eq. (47):

$$\begin{cases} 0\text{th} : \partial_t^{(1)}\phi + \partial_\alpha^{(1)}\left(u_\alpha\phi\right) = \sum_i S_{h_i}^{(1)}; \\ 1\text{st} : \partial_t^{(1)}\left(u_\alpha\phi\right) + c_s^2\partial_\alpha^{(1)}\phi - \left(1 - \frac{\Delta t}{2\tau_\phi}\right)\sum_i c_{i\alpha} S_{h_i}^{(1)} = -\frac{1}{\tau_\phi}\sum_i c_{i\alpha} h_i^{(1)}. \end{cases} \tag{50}$$

Taking the zeroth moment of Eq. (49), by the value of $\sum_i h_i^{(1)}$ and $\sum_i h_i^{(2)}$, and the first moment in Eq. (50), we have

$$\partial_\alpha^{(2)}\phi = \partial_\alpha^{(1)}\left(\tau_\phi - \frac{\Delta t}{2}\right)\left[\partial_t^{(1)}\left(u_\alpha\phi\right) + c_s^2\partial_\alpha^{(1)}\phi - \sum_i c_{i\alpha} S_{h_i}^{(1)}\right]. \tag{51}$$

Summing Eq. (51) with the zeroth moment of Eq. (50), we recover the full Allen–Cahn equation:

$$\partial_t\phi + \partial_\alpha\left(u_\alpha\phi\right) = \partial_\alpha\left[\left(\tau_\phi - \frac{\Delta t}{2}\right) c_s^2\left(\partial_\alpha\phi - \lambda n_\alpha\right)\right] + E, \tag{52}$$

which gives the relation between the mobility, M, and the relaxation time, τ_ϕ. In this equation, the remaining error is $E = -\partial_\alpha\left[\left(\tau_\phi - \frac{\Delta t}{2}\right)\epsilon^2\partial_t^{(2)}\left(u_\alpha\phi\right)\right]$.

A.2. Navier–Stokes equation

The LBE recovering the Navier–Stokes equation and the mass conservation equation uses the MRT collision operator. However, for the sake of brevity, the Chapman–Enskog analysis will be performed only considering the moments related to the target equations (NSE and mass conservation). Thus, instead of considering all the nine moments of the variables, it will be considered only the ones related to the two last relaxation rates.

First, the moments of the equilibrium distribution functions and the source term are the following,

$$\begin{cases} \sum_i g_i^{eq} = 0; \\ \sum_i c_{i\alpha} g_i^{eq} = \rho u_\alpha; \\ \sum_i c_{i\alpha}c_{i\beta} g_i^{eq} = \rho u_\alpha u_\beta + p\delta_{\alpha\beta}; \\ \sum_i c_{i\alpha}c_{i\beta}c_{i\gamma} g_i^{eq} = \rho c_s^2\left(u_\alpha\delta_{\beta\gamma} + u_\beta\delta_{\alpha\gamma} + u_\gamma\delta_{\alpha\beta}\right). \end{cases} \tag{53}$$

$$\begin{cases} \sum_i S_{g_i} = u_\alpha\partial_\alpha\rho + \rho\dot{m}'''\left(\rho_g^{-1} - \rho_l^{-1}\right); \\ \sum_i c_{i\alpha} S_{g_i} = F_\alpha; \\ \sum_i c_{i\alpha}c_{i\beta} S_{g_i} = c_s^2\left\{u_\alpha\partial_\beta\rho + u_\beta\partial_\alpha\rho + \delta_{\alpha\beta}\left[u_\gamma\partial_\gamma\rho + \rho\dot{m}'''\left(\rho_g^{-1} - \rho_l^{-1}\right)\right]\right\}. \end{cases} \tag{54}$$

Second, expanding $g_i(x_\alpha + c_{i\alpha}\Delta t, t + \Delta t)$ in Taylor series up to second order terms and substituting into de LBE, Eq. (9), we have the following expression,

$$\left(\partial_t + c_{i\alpha}\partial_\alpha\right) g_i + \frac{\Delta t}{2}\left(\partial_{tt} + 2c_{i\alpha}\partial_{t\alpha} + c_{i\alpha}^2\partial_{\alpha\alpha}\right) g_i = -\frac{1}{\tau_\nu}\left(g_i - g_i^{eq}\right) + S_{g_i}. \tag{55}$$

Expanding variables in scales of ϵ:

$$\begin{cases} g_i = g_i^{(0)} + \epsilon g_i^{(1)} + \epsilon^2 g_i^{(2)} \\ \partial_t = \epsilon\partial_t^{(1)} + \epsilon^2\partial_t^{(2)} \\ \partial_\alpha = \epsilon\partial_\alpha^{(1)} \\ S_{g_i} = \epsilon S_{sg_i}^{(1)} \end{cases} \tag{56}$$

From the scale analysis of Eq. (55), we can separate into the following equations,

$$\epsilon^0 : g_i^{(0)} = g_i^{eq}; \tag{57}$$

$$\epsilon^1 : \left(\partial_t^{(1)} + c_{i\alpha}\partial_\alpha^{(1)}\right) g_i^{(0)} = -\frac{g_i^{(1)}}{\tau_\nu} + \left(1 - \frac{\Delta t}{2\tau_\nu}\right) S_{g_i}^{(1)}; \tag{58}$$

$$\epsilon^2 : \partial_t^{(2)} g_i^{(0)} + \left(\partial_t^{(1)} + c_{i\alpha}\partial_\alpha^{(1)}\right) g_i^{(1)} + \frac{\Delta t}{2}\left(\partial_t^{(1)} + c_{i\alpha}\partial_\alpha^{(1)}\right)^2 g_i^{(0)} = -\frac{g_i^{(2)}}{\tau_\nu}. \tag{59}$$

Using Eq. (58), we can reformulate Eq. (59) as follows,

$$\partial_t^{(2)} g_i^{(0)} + \left(\partial_t^{(1)} + c_{i\alpha}\partial_\alpha^{(1)}\right)\left(1 - \frac{\Delta t}{2\tau_\nu}\right) g_i^{(1)} = -\frac{g_i^{(2)}}{\tau_\nu} - \frac{\Delta t}{2}\left(\partial_t^{(1)} + c_{i\alpha}\partial_\alpha^{(1)}\right) \times \left(1 - \frac{\Delta t}{2\tau_\nu}\right) S_{g_i}^{(1)}. \tag{60}$$

From Eq. (13), Eq. (14) and the moments of g_i^{eq} and S_{g_i}, we have:

$$\begin{cases} \sum_i g_i^{(1)} = -\frac{\Delta t}{2}\sum_i S_{g_i}^{(1)}; \\ \sum_i c_{i\alpha} g_i^{(1)} = -\frac{\Delta t}{2}\sum_i c_{i\alpha} S_{g_i}^{(1)}; \\ \sum_i g_i^{(2)} = 0; \\ \sum_i c_{i\alpha} g_i^{(2)} = 0. \end{cases} \tag{61}$$

Taking the moments of Eq. (58) and using the relations of Eq. (61),

$$\begin{cases} 0\text{th} : \partial_\alpha^{(1)}\left(\rho u_\alpha\right) = \sum_i S_{g_i}^{(1)}; \\ 1\text{st} : \partial_t^{(1)}\left(\rho u_\alpha\right) + \partial_\alpha^{(1)}\left(\rho u_\alpha u_\beta + p\delta_{\alpha\beta}\right) = \sum_i c_{i\alpha} S_{g_i}^{(1)}; \\ 2\text{nd} : \partial_t^{(1)}\left(\rho u_\alpha u_\beta + p\delta_{\alpha\beta}\right) + \partial_\alpha^{(1)}\left(\rho c_s^2 \Pi_{\alpha\beta\gamma}\right) - \left(1 - \frac{\Delta t}{2\tau_\nu}\right)\sum_i c_{i\alpha}c_{i\beta} S_{g_i}^{(1)} \\ \qquad = -\frac{1}{\tau_\nu}\sum_i c_{i\alpha}c_{i\beta} g_i^{(1)}; \end{cases} \tag{62}$$

where $\Pi_{\alpha\beta\gamma} = u_\alpha\delta_{\beta\gamma} + u_\beta\delta_{\alpha\gamma} + u_\gamma\delta_{\alpha\beta}$.

Now, taking the first moment of Eq. (60),

$$\partial_t^{(2)}\left(\rho u_\alpha\right) + \partial_\alpha^{(1)}\left(1 - \frac{\Delta t}{2\tau_\nu}\right)\sum_i c_{i\alpha}c_{i\beta} g_i^{(1)} - \frac{\Delta t}{2}\partial_\alpha^{(1)}\left(1 - \frac{\Delta t}{2\tau_\nu}\right) \times \sum_i c_{i\alpha}c_{i\beta} S_{g_i}^{(1)} = 0. \tag{63}$$

Using the 2nd moment in Eq. (62), we have

$$\partial_t^{(2)}\left(\rho u_\alpha\right) = \partial_\alpha^{(1)}\left(\tau_\nu - \frac{\Delta t}{2}\right)\left[\partial_t^{(1)}\left(\rho u_\alpha u_\beta + p\delta_{\alpha\beta}\right) + c_s^2\partial_\alpha^{(1)}\left(\rho\Pi_{\alpha\beta\gamma}\right) - \sum_i c_{i\alpha}c_{i\beta} S_{g_i}^{(1)}\right]. \tag{64}$$

Recovering the scale expansion of the 0th moment in Eq. (62), we achieve the mass conservation equation, as follows,

$$\partial_\alpha u_\alpha = \dot{m}'''\left(\rho_g - \rho_l\right) \tag{65}$$

At last, recovering the scale expansion of the 1st moment in Eqs. (62) and (64), summing both equations, using mass conservation, Eq. (65) and neglecting terms up to $O\left(\Delta t Ma^2\right)$, we achieve the NS equation if $\nu = c_s^2\rho\left(\tau_\nu - \frac{\Delta t}{2}\right)$, as follows:

$$\partial_t\left(\rho u_\alpha\right) + \partial_\alpha\left(\rho u_\alpha u_\beta\right) = -\partial_\alpha p + F_\alpha + \partial_\alpha\left[\left(\tau_\nu - \frac{\Delta t}{2}\right) c_s^2\rho\left(\partial_\alpha u_\beta + \partial_\beta u_\alpha\right)\right]. \tag{66}$$

A.3. Energy conservation equation

The Chapman–Enskog analysis for the energy equation is very similar than for the Allen–Cahn equation. The moments of the equilibrium

distribution functions and of the source term are given by Eqs. (67) and (68).

$$\begin{cases} \sum_i s_i^{eq} = T^* \\ \sum_i c_{i\alpha} s_i^{eq} = T^* u_\alpha \\ \sum_i c_{i\alpha} c_{i\beta} s_i^{eq} = c_s^2 T^* \delta_{\alpha\beta} \end{cases} \tag{67}$$

$$\begin{cases} \sum_i S_{s_i} = T^* \dot{m}''' \left(\rho_g^{-1} - \rho_l^{-1} \right) \\ \sum_i c_{i\alpha} S_{s_i} = \partial_t \left(T^* u_\alpha \right) \end{cases} \tag{68}$$

Expanding $s_i(x_\alpha + c_{i\alpha}\Delta t, t + \Delta t)$ in Taylor series, considering terms up to second order, and substituting into the thermal LBE, Eq. (22), we have:

$$\left(\partial_t + c_{i\alpha}\partial_\alpha\right) s_i + \frac{\Delta t}{2}\left(\partial_{tt} + 2c_{i\alpha}\partial_{t\alpha} + c_{i\alpha}^2\partial_{\alpha\alpha}\right) s_i = -\frac{1}{\tau_{T^*}}\left(s_i - s_i^{eq}\right) + S_{s_i}. \tag{69}$$

Expanding the variables in terms of ϵ:

$$\begin{cases} s_i = s_i^{(0)} + \epsilon s_i^{(1)} + \epsilon^2 s_i^{(2)} \\ \partial_t = \epsilon\partial_t^{(1)} + \epsilon^2\partial_t^{(2)} \\ \partial_\alpha = \epsilon\partial_\alpha^{(1)} \\ S_{s_i} = \epsilon S_{s_i}^{(1)} \end{cases} \tag{70}$$

Applying the expansion to Eq. (69), neglecting terms of order ϵ^3 and superior, and separating into the scales of ϵ, we have:

$$\epsilon^0 : s_i^{(0)} = s_i^{eq}; \tag{71}$$

$$\epsilon^1 : \left(\partial_t^{(1)} + c_{i\alpha}\partial_\alpha^{(1)}\right) s_i^{(0)} = -\frac{s_i^{(1)}}{\tau_{T^*}} + \left(1 - \frac{\Delta t}{2\tau_{T^*}}\right) S_{s_i}^{(1)}; \tag{72}$$

$$\epsilon^2 : \partial_t^{(2)} s_i^{(0)} + \left(\partial_t^{(1)} + c_{i\alpha}\partial_\alpha^{(1)}\right) s_i^{(1)} + \frac{\Delta t}{2}\left(\partial_t^{(1)} + c_{i\alpha}\partial_\alpha^{(1)}\right)^2 s_i^{(0)} = -\frac{s_i^{(2)}}{\tau_{T^*}}. \tag{73}$$

Substituting Eq. (72) into Eq. (73),

$$\partial_t^{(2)} s_i^{(0)} + \left(\partial_t^{(1)} + c_{i\alpha}\partial_\alpha^{(1)}\right)\left(1 - \frac{\Delta t}{2\tau_{T^*}}\right) s_i^{(1)} = -\frac{s_i^{(2)}}{\tau_{T^*}} - \frac{\Delta t}{2}\left(\partial_t^{(1)} + c_{i\alpha}\partial_\alpha^{(1)}\right) \times \left(1 - \frac{\Delta t}{2\tau_{T^*}}\right) S_{s_i}^{(1)}. \tag{74}$$

To determine the moments of $s_i^{(1)}$ and $s_i^{(2)}$, we start from Eq. (25), Eq. (67) and (68). Similarly to Appendix A.1, we have that $\sum_i s_i^{(1)} = -\Delta t/2 \sum_i S_{s_i}^{(1)}$ and $\sum_i s_i^{(2)} = 0$. Then, taking the zeroth and first moments of Eq. (72),

$$\begin{cases} 0\text{th} : \partial_t^{(1)} T^* + \partial_\alpha^{(1)}\left(u_\alpha T^*\right) = \sum_i S_{h_i}^{(1)}; \\ 1\text{st} : \partial_t^{(1)}\left(u_\alpha T^*\right) + c_s^2\partial_\alpha^{(1)} T^* - \left(1 - \frac{\Delta t}{2\tau_{T^*}}\right)\sum_i c_{i\alpha} S_{s_i}^{(1)} = -\frac{1}{\tau_{T^*}}\sum_i c_{i\alpha} s_i^{(1)}. \end{cases} \tag{75}$$

Next, taking the zeroth moment of Eq. (73), using the first moment of Eq. (75) and the relations found for $\sum_i s_i^{(1)}$ and $\sum_i s_i^{(2)}$,

$$\partial_\alpha^{(2)} T^* = \partial_\alpha^{(1)}\left(\tau_{T^*} - \frac{\Delta t}{2}\right)\left[\partial_t^{(1)}\left(u_\alpha T^*\right) + c_s^2\partial_\alpha^{(1)} T^* - \sum_i c_{i\alpha} S_{s_i}^{(1)}\right]. \tag{76}$$

Summing Eq. (76) with the zeroth moment in Eq. (75), and recovering the scale analysis, we have:

$$\partial_t T^* + \partial_\alpha\left(u_\alpha T^*\right) = \partial_\alpha\left[\left(\tau_{T^*} - \frac{\Delta t}{2}\right) c_s^2\partial_\alpha T^*\right] + \dot{m}''' T^*\left(\rho_g^{-1} - \rho_l^{-1}\right) + E, \tag{77}$$

From the continuity equation, Eq. (65), and with the relation $\alpha_l = \left(\tau_{T^*} - \frac{\Delta t}{2}\right) c_s^2$, we achieve the full energy equation, Eq. (78), with the error term $E = -\partial_\alpha\left[\left(\tau_{T^*} - \frac{\Delta t}{2}\right)\epsilon^2\partial_t^{(2)}\left(u_\alpha T^*\right)\right]$.

$$\partial_t T^* + u_\alpha\partial_\alpha T^* = \partial_\alpha\left(\alpha_l\partial_\alpha T^*\right) + E \tag{78}$$

A.4. Forces calculation

In this section we present the models used here for the forces estimation, both for numerical and experimental [72]. The scheme used are based on Zeng et al. [99] proposition.

Starting by the buoyancy force, the same is calculated by the traditional way, considering the bubble volume, the gravitational acceleration and the density difference between gas and liquid phases, as given in Eq. (79).

$$F_b(t) = V(t)(\rho_l - \rho_g)|\mathbf{g}| \tag{79}$$

Next, for the surface tension force, the authors proposed the expression given by Eq. (80), where σ is the surface tension value, R_d is the dry radius and φ_{ap} is the apparent contact angle.

$$F_\sigma(t) = -2\pi R_d(t)\sigma\sin\left(\varphi_{ap}(t)\right) \tag{80}$$

The contact pressure are related to the pressure inside the bubble. Zeng et al. [99] proposed the form given by Eq. (81), where R_r is the radius of curvature at the base of the bubble. In this case, we followed the suggestion of the mentioned authors, in which $R_r \approx 5R_{eq}$.

$$F_{cp}(t) = \pi R_d(t)^2\frac{2\sigma}{R_r(t)}; \tag{81}$$

At last, the forces related to the growth resistance and lift (both drag forces) because of the movement between the liquid and the bubble, as well as the added mass force (also related to the growth process) are included in a single force called "dynamic force". As we have the position of the bubble center of mass with time, we can estimate its velocity (v) and, consequently, its acceleration. Thus, we can estimate the resultant force acting on the bubble. By a force balance, we can then estimate the value of the dynamic force, given by Eq. (82).

$$F_D(t) = -\rho_g V(t)\frac{dv(t)}{dt} + F_b(t) + F_\sigma(t) + F_{cp}(t); \tag{82}$$

The previous expressions were used for estimating the forces acting on the numerical bubble. For a more detailed explanation, see Martins et al. [72].

Appendix B. Supplementary data

Supplementary material related to this article can be found online at https://doi.org/10.1016/j.icheatmasstransfer.2025.109207.

Data availability

Data will be made available on request.

References

[1] V.P. Carey, Liquid-Vapor Phase-Change Phenomena: An Introduction to the Thermophysics of Vaporization and Condensation Processes in Heat Transfer Equipment, third ed., CRC Press, 2020.

[2] S. Succi, The Lattice Boltzmann Equation: for Complex States of Flowing Matter, Oxford University pressSpringer-Verlag, 2018.

[3] D.A. Wolf-Gladrow, Lattice-Gas Cellular Automata and Lattice Boltzmann Models: An Introduction, Springer-Verlag, 2002.

[4] T. Krüger, H. Kusumaatmaja, A. Kuzmin, O. Shardt, G. Silva, E. Viggen, The Lattice Boltzmann Method: Principles and Practice, Springer International Publishing, 2017.

[5] D.H. Rothman, J.M. Keller, Immiscible cellular-automaton fluids, J. Stat. Phys. 82 (3–4) (1981) 1119–1127.

[6] A.K. Gunstensen, D.H. Rothman, S. Zaleski, G. Zanetti, Lattice Boltzmann model of immiscible fluids, Phys. Rev. A 43 (8) (1991) 4320.

[7] D. Grunau, S. Chen, K. Eggert, A lattice Boltzmann model for multiphase fluid flows, Phys. Fluids A 5 (10) (1993) 2557–2562.

[8] X. Shan, H. Chen, Lattice Boltzmann model for simulating flows with multiple phases and components, Phys. Rev. E 47 (1993) 1815.

[9] X. Shan, H. Chen, Simulation of nonideal gases and liquid-gas phase transitions by the lattice Boltzmann equation, Phys. Rev. E 49 (1994) 2941.

[10] X. Shan, G. Doolen, Multicomponent lattice-Boltzmann model with interparticle interaction, J. Stat. Phys. 81 (1995) 379–393.

[11] M.R. Swift, W.R. Osborn, J.M. Yeomans, Lattice Boltzmann simulations of non-ideal fluids, Phys. Rev. Lett. 75 (5) (1995) 830–833.

[12] E. Orlandini, M.R. Swift, J.M. Yeomans, Lattice Boltzmann model of of binary-fluid mixtures, Europhys. Lett. 32 (6) (1995) 463–468.

[13] M.R. Swift, E. Orlandini, W.R. Osborn, J.M. Yeomans, Lattice Boltzmann simulations of liquid-gas and binary fluid systems, Phys. Rev. E 54 (5) (1996) 5041–5052.

[14] X. He, S. Chen, R. Zhang, A lattice Boltzmann scheme for incompressible multiphase flow and its application in simulation of Rayleigh–taylor instability, J. Comput. Phys. 152 (1999) 642–663.

[15] T. Inamuro, T. Ogata, F. Ogino, Numerical simulation of bubble flows by the lattice Boltzmann method, Future Gener. Comput. Syst. 20 (2004) 959–964.

[16] H.W. Zheng, C. Shu, Y.T. Chew, A lattice Boltzmann model for multiphase flows with large density ratio, J. Comput. Phys. 218 (2006) 353–371.

[17] T. Lee, C.L. Lin, A stable discretization of the lattice Boltzmann equation for simulation of incompressible two-phase flows at high density ratio, J. Comput. Phys. 206 (2005) 16–47.

[18] H. Liu, Q. Kang, C.R. Leonardi, S. Schmieschek, A. Narváez, B.D. Jones, J.R. Williams, A.J. Valocchi, J. Harting, Multiphase lattice Boltzmann simulations for porous media applications: A review, Comput. Geosci. 20 (2016) 777–805.

[19] K.N. Premnath, M. McCracken, J. Abraham, A review of lattice Boltzmann methods for multiphase flows relevant to engine sprays, SAE Tech. Pap. Ser. 01 (2005) 0996.

[20] Q. Li, K. Luo, Q. Kang, Y. He, Q. Chen, Q. Liu, Lattice Boltzmann methods for multiphase flow and phase-change heat transfer, Prog. Energy Combust. Sci. 52 (2016) 62–105.

[21] Y.T. Mu, L. Chen, Y.L. He, Q.J. Kang, W.Q. Tao, Nucleate boiling performance evaluation of cavities at mesoscale level, Int. J. Heat Mass Transfer 106 (2017) 708–719.

[22] S. Gong, P. Cheng, Direct numerical simulations of pool boiling curves including heater's thermal responses and the effect of vapor phase's thermal conductivity, Int. Commun. Heat Mass Transfer 87 (2017) 61–71.

[23] E.O. Fogliatto, A. Clausse, F.E. Teruel, Development of a double-MRT pseudopotential model for tridimensional boiling simulation, Int. J. Therm. Sci. 179 (2022) 107637.

[24] H. Liang, W. Liu, Y. Li, Y. Wei, A thermal lattice Boltzmann model for evaporating multiphase flows, Phys. Fluids 36 (3) (2024) 032101.

[25] C. Zhang, L. Chen, W. Ji, Y. Liu, L. Liu, W.Q. Tao, Lattice Boltzmann mesoscopic modeling of flow boiling heat transfer processes in a microchannel, Appl. Therm. Eng. 197 (2021) 117369.

[26] Y. Song, X. Mu, J. Wang, S. Shen, G. Liang, Channel flow boiling on hybrid wettability surface with lattice Boltzmann method, Appl. Therm. Eng. 233 (2023) 121191.

[27] J. Li, D.V. Le, H. Li, X. Zhang, C.W. Kang, J. Lou, Hybrid outflow boundary condition for the pseudopotential LBM simulation of flow boiling, Int. J. Therm. Sci. 196 (2024) 108741.

[28] M.J. Sayyari, M.H. Ahmadian, K.C. Kim, Three-dimensional condensation in a vertical channel filled with metal foam using a pseudo-potential lattice Boltzmann model, Int. J. Therm. Sci. 172 (2022) 107352.

[29] H. Peng, J. Zhang, X. He, Y. Wang, Thermal pseudo-potential lattice Boltzmann method for simulating cavitation bubbles collapse near a rigid boundary, Comput. & Fluids 217 (2021) 104817.

[30] J.D. Yao, K. Luo, J. Wu, H.L. Yi, Electrohydrodynamic effects on bubble dynamics during nucleate pool boiling under the leaky dielectric assumption, Phys. Fluids 34 (1) (2022) 013606, http://dx.doi.org/10.1063/5.0077313, arXiv:https://pubs.aip.org/aip/pof/article-pdf/doi/10.1063/5.0077313/16617947/013606_1_online.pdf.

[31] J.D. Yao, K. Luo, J. Wu, H.L. Yi, H.P. Tan, Effect of electric field on bubble dynamics in channel flow boiling using lattice Boltzmann method, Int. J. Heat Fluid Flow 109 (2024) 109550, http://dx.doi.org/10.1016/j.ijheatfluidflow.2024.109550, URL: https://www.sciencedirect.com/science/article/pii/S0142727X24002753.

[32] A. Jaramillo, V.P. Mapelli, L. Cabezas-Gómez, Pseudopotential lattice Boltzmann method for boiling heat transfer: a mesh refinement procedure, Appl. Therm. Eng. 213 (2022) 118705.

[33] S.C. Wang, Z.X. Tong, Y.L. He, X. Liu, Unit conversion in pseudopotential lattice Boltzmann method for liquid–vapor phase change simulations, Phys. Fluids 34 (10) (2022) 103305.

[34] G. Wang, L. Fei, K.H. Luo, Unified lattice Boltzmann method with improved schemes for multiphase flow simulation: Application to droplet dynamics under realistic conditions, Phys. Rev. E 105 (4) (2022) 045314.

[35] W. Zheng, F. Hong, S. Gong, Improved multi-relaxation time thermal pseudopotential lattice Boltzmann method with multi-block grid and complete unit conversion for liquid–vapor phase transition, Phys. Fluids 35 (5) (2023) 053337.

[36] I.T. Martins, P.F. Alvariño, L. Cabezas-Gómez, Lattice Boltzmann method for simulating transport phenomena avoiding the use of lattice units, J. Braz. Soc. Mech. Sci. Eng. 46 (2024) 333.

[37] G. Gonnella, E. Orlandini, J.M. Yeomans, Spinodal decomposition to a lamellar phase: Effects of hydrodynamic flow, Phys. Rev. Lett. 78 (9) (1997) 1695–1698.

[38] V.M. Kendon, J.C. Desplat, P. Bladon, M.E. Cates, 3D spinodal decomposition in the inertial regime, Phys. Rev. Lett. 83 (3) (1999) 576–579.

[39] A. Lamura, G. Gonnella, Lattice Boltzmann simulations of segregating binary fluid mixtures in shear flow, Physica A 294 (2001) 295–312.

[40] V.M. Kendon, M.E. Cates, I. Pagonabarraga, J.-C. Desplat, P. Blandon, Inertial effects in three-dimensional spinodal decomposition of a symmetric binary fluid mixture: a lattice Boltzmann study, J. Fluid Mech. 440 (2001) 147–203.

[41] J.C. Desplat, I. Pagonabarraga, P. Bladon, LUDWIG: A parallel Lattice-Boltzmann code for complex fluids, Comput. Phys. Comm. 134 (2001) 273–290.

[42] A.J. Briant, P. Papatzacos, J.M. Yeomans, Lattice Boltzmann simulations of contact line motion in a liquid–gas system, Phil. Trans. R. Soc. Lond. A 360 (2002) 485–495.

[43] A.J. Briant, A.J. Wagner, J.M. Yeomans, Lattice Boltzmann simulations of contact line motion. I. Liquid-gas systems, Phys. Rev. E 69 (2004) 031602.

[44] A.J. Bray, Theory of phase ordering kinetics, Adv. Phys. 43 (3) (1994) 357–459.

[45] Z. Dong, W. Li, Y. Song, Lattice Boltzmann simulation of growth and deformation for a rising vapor bubble through superheated liquid, Numer. Heat Transf. Part A 55 (2009) 381–400.

[46] Z. Dong, W. Li, Y. Song, A numerical investigation of bubble growth on and departure from a superheated wall by lattice Boltzmann method, Int. J. Heat Mass Transfer 53 (21) (2010) 4908–4916.

[47] T. Sun, W. Li, S. Yang, Numerical simulation of bubble growth and departure during flow boiling period by lattice Boltzmann method, Int. J. Heat Fluid Flow 44 (2013) 120–129.

[48] T. Sun, A numerical study on dynamics behaviors of multi bubbles merger during nucleate boiling by lattice Boltzmann method, Int. J. Heat Fluid Flow 118 (2019) 128–140.

[49] A. Fakhari, M.H. Rahimian, Phase-field modeling by the method of lattice Boltzmann equations, Phys. Rev. E 81 (2010) 036707.

[50] H. Liang, J. Xu, J. Chen, H. Wang, Z. Chai, B. Shi, Phase-field-based lattice Boltzmann modeling of large-density-ratio two-phase flows, Phys. Rev. E 98 (2018) 033301.

[51] Y.Q. Zu, S. He, Phase-field-based lattice Boltzmann model for incompressible binary fluid systems with density and viscosity contrasts, Phys. Rev. E 87 (2013) 043301.

[52] T. Lee, C.L. Lin, L.D. Chen, A lattice Boltzmann algorithm for calculation of the laminar jet diffusion flame, J. Comput. Phys. 215 (2006) 133–152.

[53] T. Lee, P.F. Fischer, Eliminating parasitic currents in the lattice Boltzmann equation method for nonideal gases, Phys. Rev. E 74 (2006) 046709.

[54] L. Amaya-Bower, T. Lee, Single bubble rising dynamics for moderate Reynolds number using Lattice Boltzmann Method, Comput. & Fluids 39 (2010) 1191–1207.

[55] T. Lee, Effects of incompressibility on the elimination of parasitic currents in the lattice Boltzmann equation method for binary fluids, Comput. Math. Appl. 58 (2009) 987–994.

[56] T. Lee, L. Liu, Lattice Boltzmann simulations of micron-scale drop impact on dry surfaces, J. Comput. Phys. 229 (2010) 8045–8063.

[57] H. Safari, M.H. Rahimian, M. Krafczyk, Extended lattice Boltzmann method for numerical simulation of thermal phase change in two-phase fluid flow, Phys. Rev. E 88 (2013) 013304.

[58] H. Safari, M.H. Rahimian, M. Krafczyk, Consistent simulation of droplet evaporation based on the phase-field multiphase lattice Boltzmann method, Phys. Rev. E 90 (2014) 033305.

[59] A. Begmohammadi, M. Farhadzadeh, M.H. Rahimian, Simulation of pool boiling and periodic bubble release at high density ratio using lattice Boltzmann method, Int. Commun. Heat Mass Transf. 61 (2015) 78–87.

[60] R. Sadeghi, M.S. Shadloo, M.Y.A. Jamalabadi, A. Karimipour, A three-dimensional lattice Boltzmann model for numerical investigation of bubble growth in pool boiling, Int. Commun. Heat Mass Transf. 79 (2016) 58–66.

[61] Q. Lou, Z.L. Guo, B.C. Shi, Effects of force discretization on mass conservation in lattice Boltzmann equation for two-phase flows, Europhys. Lett. 99 (6) (2013) 64005.

[62] A. Fakhari, M. Geierb, T. Lee, A mass-conserving lattice Boltzmann method with dynamic grid refinement for immiscible two-phase fows, J. Comput. Phys. 315 (2016) 434–457.

[63] A. Fakhari, D. Bolstera, L.S. Luo, A weighted multiple-relaxation-time lattice Boltzmann method for multiphase flows and its application to partial coalescence cascades, J. Comput. Phys. 341 (2017) 22–43.

[64] H. Liang, H. Liu, Z. Chai, B. Shi, Lattice Boltzmann method for contact-line motion of binary fluids with high density ratio, Phys. Rev. E 99 (2019) 063306.

[65] S. Zhang, J. Tang, H. Wu, Phase-field lattice Boltzmann model for two-phase flows with large density ratio, Phys. Rev. E 105 (2022) 015304.

[66] R. Haghani-Hassan-Abadi, A. Fakhari, M.H. Rahimian, Phase-change modeling based on anovel conservative phase-field method, J. Comp. Phys. 432 (2021) 110111.

[67] Q. He, W. Huang, Y. Yin, D. Li, Y. Wang, A lattice Boltzmann model for liquid-vapor-solid flow with thermal phase change, Comput. Math. Appl. 114 (2022) 60–72.

[68] J. Bi, D.M. Christopher, D. Zhao, J. Xu, Y. Huang, Numerical study of bubble growth and merger characteristics during nucleate boiling, Prog. Nucl. Energy 112 (1) (2019) 7–19.
[69] Q. Kong, B. Dong, Y. Zhang, X. An, W. Li, Effects of surface characteristics on bubble dynamics in nucleation boiling using LBM, Int. J. Therm. Scicences 197 (1) (2024) 108838.
[70] Z. Xu, J. Qin, X. Ma, Experimental and numerical investigation on bubble behaviors and pool boiling heat transfer of semi-modified copper square pillar arrays, Int. J. Therm. Sci. 160 (1) (2021) 106680.
[71] P.F. Alvariño, M.L.S. Simón, M. dos Santos Guzella, J.M.A. Paz, J.M.S. Jabardo, L.C. Gómez, Experimental investigation of the CHF of HFE-7100 under pool boiling conditions on differently roughened surfaces, Int. J. Heat Mass Transfer 139 (2019) 269–279.
[72] I.T. Martins, P. Fariñas Alvariño, L. Cabezas-Gómez, A new methodology for experimental analysis of single-cavity bubble's nucleation, growth and detachment in saturated HFE-7100, Exp. Therm. Fluid Sci. 159 (2024) 111272.
[73] M. Sugimoto, Y. Sawada, M. Kaneda, K. Suga, Consistent evaporation formulation for the phase-field lattice Boltzmann method, Phys. Rev. E 103 (2021) 053307.
[74] S.M. Ghiaanian, Two-Phase Flow, Boiling and Condensation in Conventional and Miniature Systems, Cambridge University Press, 2008.
[75] S.R. de Groot, P. Mazur, Non-equilibrium Thermodynamics, Dover Publications, INC., New York, 1984.
[76] M. Geier, A. Fakhari, T. Lee, Conservative phase-field lattice Boltzmann model for interface tracking equation, Phys. Rev. E 91 (2015) 063309.
[77] S. Chapman, T.G. Cowling, The Mathematical Theory of Non-uniform Gases, second ed., Cambridge University Press, 1952.
[78] Y.H. Qian, D. D'Humieres, P. Lalleman, Lattice BGK models for Navier-Stokes equation, Europhys. Lett. 17 (6) (1992) 479–484.
[79] L.E. Czelusniak, L. Cabezas-Gómez, A.J. Wagner, Effect of gravity on phase transition for liquid–gas simulations, Phys. Fluids 35 (4) (2023) 043324.
[80] C. Zhang, Z. Guo, L.P. Wang, Improved well-balanced free-energy lattice Boltzmann model for two-phase flow with high Reynolds number and large viscosity ratio, Phys. Fluids 34 (1) (2022) 012110.
[81] N. Karami, M.H. Rahimian, M. Farhadzadeh, Numerical simulation of droplet evaporation on a hot surface near leidenfrost regime using multiphase lattice Boltzmann method, Appl. Math. Comput. 312 (2017) 91–108.
[82] J.R. Thome, J. Kim, Encyclopedia of Two-Phase Heat Transfer and Flow II: Numerical modeling of two-phase flow and heat transfer, World Scientific, 2016.
[83] D. Jacqmin, Calculation of two-phase Navier–Stokes flows using phase-field modeling, J. Comput. Phys. 155 (1999) 96–127.
[84] F. Ren, B. Song, M.C. Sukop, H. Hu, Improved lattice Boltzmann modeling of binary flow basedon the conservative Allen–Cahn equation, Phys. Rev. E 94 (2016) 023311.
[85] L.E. Reichl, A Modern Course in Statiscical Physics, second ed., John Wiley & Sons, Inc., 1998.
[86] D. Jamet, O. Lebaigue, N. Coutris, J.M. Delhaye, The second gradient method for the direct numerical simulation of liquid–vapor flows with phase change, J. Comput. Phys. 169 (2001) 624–651.
[87] L. Bures, M. Bucci, Y. Sato, M. Bucci, A coarse grid approach for single bubble boiling simulations with the volume of fluid method, Comput. & Fluids 271 (2024) 106182.
[88] A.J.C. Ladd, Numerical simulations of particulate suspensions via a discretized Boltzmann equation. Part 1. Theoretical foundation, J. Fluid Mech. 271 (1994) 285–309.
[89] A.J.C. Ladd, R. Verberg, Lattice-Boltzmann simulations of particle-fluid suspensions, J. Stat. Phys. 104 (5–6) (2001) 1191–1251.
[90] I. Ginzburg, Generic boundary conditions for lattice Boltzmann models and their application to advection and anisotropic dispersion equations, Adv. Water Resour. 28 (2005) 1196–1216.
[91] A.A. Mohamad, Lattice Boltzmann Method: Fundamentals and Engineering Applications with Computer Codes, Springer-Verlag London Ltd., part of Spring Nature, 2019.
[92] P.G. de Gennes, Wetting: statics and dynamics, Rev. Modern Phys. 57 (1985) 827–863.
[93] T. Young, III. An essay on the cohesion of fluids, Philos. Trans. R. Soc. 95 (1805) 65–87.
[94] S.A. Klein, EES – engineering equation solver version 11.444 (2022-09-29), 2022, URL: https://fchartsoftware.com/, Computer Software.
[95] S. Saito, A. De Rosis, L. Fei, K.H. Luo, K.i. Ebihara, A. Kaneko, Y. Abe, Lattice Boltzmann modeling and simulation of forced-convection boiling on a cylinder, Phys. Fluids 33 (2) (2021) 023307.
[96] M. Mirhoseini, A. Banaee, A. Jalali, A novel phase-field lattice Boltzmann framework for diffusion-driven multiphase evaporation, Phys. Fluids 36 (8) (2024) 083314.
[97] A. Stalder, G. Kulik, D. Sage, L. Barbieri, P. Hoffmann, A snake-based approach to accurate determination of both contact points and contact angles, Colloids Surfaces A: Physicochemical Eng. Asp. 286 (1–3) (2006) 92–103.
[98] C.-Y. Han, P. Griffith, The Mechanism of Heat Transfer in Nucleate Pool Boiling, Technical Report 7673–19, Department of Mechanical Engineering, Massachusetts Institute of Technology, Cambridge 39, Massachusetts, 1962.
[99] L.Z. Zeng, J.F. Klausner, R. Mei, A unified model for the prediction of bubble detachment diameters in boiling systems-I. Pool boiling, Int. J. Heat Mass Transfer 36 (9) (1993) 2261–2270.